Hydrodynamic and mass transfer in inertial gas–liquid flow regimes through straight and meandering millimetric square channels

Matthieu Roudet, Karine Loubière, Christophe Gourdon, Michel Cabassud

Hydrodynamic and mass transfer in inertial gas–liquid flow regimes through straight and meandering millimetric square channels

Matthieu Roudet [a,c], Karine Loubiere [a,c,*], Christophe Gourdon [a,c], Michel Cabassud [b,c]

[a] Université de Toulouse, INPT, UPS, Laboratoire de Génie Chimique, 4 allée Emile Monso, BP 84234, F-31030 Toulouse, France
[b] Université de Toulouse, INPT, UPS, Laboratoire de Génie Chimique, 137 avenue de Rangueil, BP 67701, F-31077 Toulouse cedex 4, France
[c] CNRS, Laboratoire de Génie Chimique, F-31062 Toulouse, France

A B S T R A C T

Heat-exchanger reactors are an important part of process intensification technology. For plate geometries, one solution for intensifying transfer and increasing residence times is to construct two-dimensional meandering channels. Supported by this scientific context, the present work aims at characterising gas–liquid mass transfer in the same square millimetric meandering channel, as in Anxionnaz (2009), this constituted the preliminary step required for performing exothermic gas–liquid reactions. Firstly, the gas–liquid hydrodynamics were characterised for a water/air system. When compared to a straight channel of identical compactness and sectional-area ($2 \times 2\ mm^2$), the meandering channel induced (i) a delay in the transition from Taylor to annular-slug regimes, (ii) a rise of 10–20% in bubble lengths while conserving almost identical slug lengths, (iii) higher deformations of bubble nose and rear due to centrifugal forces (bends). Secondly, an original method for verifying the relevancy of the plug flow model and accurately determining $k_l a$ was used (measurements of concentrations in dissolved oxygen along the channel length). For the Taylor flow regime, $k_l a$ increased coherently when increasing j_g, and the meandering geometry had a small influence. On the contrary, this effect was found no more negligible for the slug-annular flow regime. Whatever the channels, the NTU_l remained low, thus showing that, even if millimetric channels allowed to intensify $k_l a$, a special attention should be paid for generating sufficient residence times. At identical compactness, the meandering channel was found to be the most competitive. Finally, results on gas–liquid interfacial areas and mass transfer coefficients were confronted and discussed with respect to the predictions issued from the model developed by Van Baten and Krishna (2004).

1. Introduction

Heat-exchanger reactors (HEX) are an important part of process intensification technology, as regrouping many benefits (Stankiewicz and Moulijn, 2000; Ferrouillat et al., 2006; Anxionnaz et al., 2008, 2010): high selectivity and yields due to heat and mass transfer enhancement and flow structure (plug flow behaviour), minimised risk of runaway reactions due to enhanced heat transfer and smaller sizes, reduction of waste of energy and raw materials, smaller and cheaper plant. As they are above all heat-exchangers carrying out reactions, their design is largely based on compact heat-exchanger geometries, in which metallic foams, fins, etc., can be inserted to improve reaction conditions (mixing, residence time, etc.). An interesting overview of the different designs of HEX reactors is given in Anxionnaz et al. (2008). Among various challenges posed by such technology, two remain particularly important for industrial purposes: how can plug flow be combined with residence times sufficiently high for chemistry? How can laminar regimes be associated with heat and mass transfer intensification? One solution is to generate instationnarities or chaos (required for intensified transfers), while working with flows characterised by laminar regimes (required for high residence times). By inducing secondary recirculations (Dean flows), the use of 2D meandering channel structures constitutes a promising way to reach these objectives. Based on this background, Anxionnaz (2009) investigated the effect of geometric parameters (channel aspect ratio, bend angle, bend curvature radius, bend straight length) on thermo-hydraulic performances (pressure drop, residence time distribution, mixing, heat transfer coefficient) of a plate heat-exchanger reactor involving meandering millimetric channels. In particular, they converged towards optimal geometries as a function of application constraints in the case of one-phase reactive flows. For two-phase

* Corresponding author at: Université de Toulouse, INPT, UPS, Laboratoire de Génie Chimique, 4 allée Emile Monso, BP 84234, F-31030 Toulouse, France. Tel: +33 5 34 32 36 19.
E-mail address: Karine.Loubiere@ensiacet.fr (K. Loubiere).

reactions (liquid–liquid or gas–liquid), no specific investigation has been out carried at present.

In keeping with this scientific context, the present work aims at characterising gas–liquid mass transfer in the same meandering millimetric channels as Anxionnaz (2009); this will constitute the preliminary step required for performing exothermic gas–liquid reactions in plate heat-exchanger reactors. Indeed, such two-phase systems still raise many fundamental questions, in particular when chemical reactions are involved. Mass transfer between both phases plays then a key role, and, depending on chemical kinetics, can become the limiting step controlling the chemical reaction. In this case, the knowledge of gas–liquid hydrodynamics (i.e. flow regime, mixing, interfacial area), which is affected by the geometry of the millimetric channel (straight or meandering), is crucial for predicting mass transfer properties and in return chemical conversion/selectivity.

For many years, gas–liquid flows in millimetric channels (mainly in capillaries with flow-focusing gas injection devices) are the object of intensive literature (for example, Banerjee et al., 1970; Barnea et al., 1983; Thulasidas et al., 1997; Kreutzer et al., 2003; Taha and Cui, 2006). Especially for multiphase monoliths applications, special attention has been paid to the bubble-train flow of elongated bubbles as being the predominant flow pattern, representing a classical problem in fluid mechanics referred to as 'Bretherton's problem' (Bretherton, 1961) or 'Taylor flow' (Taylor, 1961), but also as allowing good mass-transfer rates from bubbles to liquid. Bercic and Pintar (1997) studied gas–liquid mass transfer in capillaries under Taylor flow regime: they correlated by a simple correlation the influence of capillary diameter, unit cell length and gas hold-up on measured volumetric mass transfer coefficients (k_la); in their conditions, the mass transport was mostly determined by liquid slug length and velocity while the contribution of the thin liquid film surrounding gas bubbles was not dominant. Computational fluid dynamics (CFD) was used by Van Baten et al. (2004) to investigate mass transfer from Taylor bubbles to the liquid phase in circular capillaries (1.5–3 mm in diameter); they outlined that the mass transfer from Taylor bubbles was the sum of the contributions of the two bubble caps and the film surrounding the bubbles. The model for k_la they developed was based on the Higbie penetration model (Higbie, 1935) and the unsteady-state diffusion model of Pigford (Sherwood et al., 1975) to describe mass transfer from the two hemispherical caps and from the downward flowing liquid, respectively. Tortopidis and Bontozoglou (1997) extended mass transfer investigations from the Taylor flow to annular flow regimes (vertical capillary, 4 mm in internal diameter); they measured volumetric mass transfer coefficients k_la by absorption of CO_2 into NaOH solution and showed that (i) k_la increased when increasing gas superficial velocity j_g (at a fixed liquid superficial velocity j_l), and that (ii) annular flow provided the highest values of k_la.

Increasingly, the benefits of Taylor flow in millimetric capillaries have been recognised outside the field of monoliths, especially in microfluidics and microreactor community (Hessel et al., 2005; Kreutzer et al., 2005; Su et al., 2010; Shao et al., 2010). Recently, Yue et al. (2007) observed in a horizontal rectangular channel ($1000 \times 500\ \mu m^2$) (i) intensified volumetric mass transfer coefficients ($0.3 < k_la < 21\ s^{-1}$) when compared to other efficient gas–liquid contactors, and (ii) a clear increase of k_la with j_g for Taylor regime until reaching a constant value for slug-annular flow. Fries et al. (2008) used optical methods such as laser induced fluorescence (LIF) and confocal laser scanning microscopy (LSM) to access local gas–liquid phase distributions in rectangular microchannels, this information being crucial for mass transfer analysis; they demonstrated that (i) the film thickness in channel corners slightly decreased with Ca, (ii) for low Ca, the film thickness at walls stayed nearly constant, and (iii) the contribution of the film in corners to the total film area was about 70%.

Most of the works reported consider straight channels; few works are surprisingly devoted to gas–liquid mass transfer in meandering channels even if the latter are desirable as mixers for creating long channels at a small chip size and for generating some special flow effects providing enhanced mixing. Various concepts for improving two-phase mixing are discussed in literature (Hardt et al., 2005; Nguyen and Wu, 2005). In general, the influence of curved channels on the flow is known to differ from one-phase to two-phase flows: in one-phase flows, the so called Dean flow is observed for high Re, while in two-phase flows, the asymmetrical recirculations generated in the Taylor flow regime increase transfer phenomena. Recently, Dessimov et al. (2010) investigated the influence of non-straight channels (Y-shaped chicane mixer with circular cross-section) on flow patterns and flow regime transitions; quantitative criteria were proposed to predict slug and annular flow domains independently on the inlet geometries, reactor material, its cross-section shape and liquid phase properties. To study mixing in liquid slugs, Fries et al. (2009) carried out μ-PIV measurements in meandering microchannels with Dean numbers larger than the unity; they demonstrated that the liquid velocity field in segmented gas–liquid flow depended strongly on channel geometry (curve radii, channel diameter) and on superficial velocity rates. Indeed, when passing channel bends, liquid was transported due to centrifugal forces from the inner channel halve to the outer one and transported back by the recirculation. In addition, these authors showed that an increase of superficial liquid velocities allowed enhancing this asymmetric motion. All these works confirm the idea that an intensification of mass transfer is possible by using meandering channels.

In this study, we focus on gas–liquid mass transfer in a meandering millimetric channel of square section (2 mm × 2 mm), for flow regimes evolving from Taylor flow to slug-annular flow. For comparison, a straight channel of identical cross-sectional area and compactness in length is also investigated. Firstly, gas–liquid hydrodynamics is characterised in both channels for a water/air system, namely flow regime and bubble shape, flow structure, bubble length and velocity. For the Taylor flow regime, the bubbles move at high Reynolds numbers and the Dean number of the meandering channel is always much larger than the unity.

The second part is dedicated to the study of mass transfer from gas phase to liquid phase. For this purpose, we use an original method where variation of concentrations in dissolved oxygen into permute water is measured along the channel length. The usual methods for measuring k_la consist in fitting concentrations at the inlet and outlet of the channel by means of the relationship derived from the plug flow model (Irandoust and Andersson, 1988; Bercic and Pintar, 1997; Kreutzer et al., 2003). Here, the present method offers the advantage to verify the relevancy of the plug flow model, and thus to determine more accurately the volumetric mass transfer coefficients k_la. A comparison between straight and meandering channels is afterwards performed, in terms of k_la, absorption efficiency and number of transfer units. Finally, the results obtained are compared to the predictions issued from the model developed by Van Baten and Krishna (2004).

2. Material and methods

2.1. Description of the experimental set-up

The experimental set-up consists of two horizontal channels of square section $A = l^2$ where $l = 2$ mm. The first channel is a straight

channel of 0.24 m in length and the second one is a periodic meandering channel with a radius of curvature of 1.5 mm, a straight length between two bends of 6.94 mm and a total developed straight length of 0.34 m (Fig. 1). Both channels have the same compactness in length. Note that the geometrical characteristics of this meandering channel result from the work of Anxionnaz (2009) who investigated the effect of channel geometry on the thermal–hydraulic performances in a plate heat-exchanger reactor. Each channel is carved in a plate (0.03 m in thickness) made of polymethyl methacrylate (PMMA) and roofed over in a watertight manner by an other plate (0.03 m in thickness). As the wetting properties of the channel material can affect the two-phase flow patterns (Barajas and Panton, 1993), it is interesting to mention that the present channel material (i.e. PMMA) is partially wetting/hydrophilic, with a water contact angle of about 70°. Holes of diameter 1.6 mm are pierced perpendicular to each channel in the carved plate at different distances X from the exit (Fig. 2): for the straight channel, X is equal to 0.02, 0.07, 0.12, 0.17 and 0.22 m, and for the meandering one, X is equal to 0.02, 0.07, 0.12, 0.17, 0.22 and 0.32 m (Fig. 1). The liquid phase is injected at the furthest point of each channel, so at $X=0.24$ m and at $X=0.34$ m for the straight and meandering channels, respectively. On the contrary, the gas phase can be injected from one of the other holes, namely at different distances X from the channel exit. Before entering in the main channel, the gas phase flows through a winding of a 2 m long capillary of 750 μm internal diameter, aiming at increasing pressure drop and thus creating stable gas injection in the liquid stream. Stoppers of metal are inserted inside injection holes unused for injecting gas in order to minimise the dead volume of liquid. They are located at 0.5 mm from the inside of the main channel to prevent any minor disturbance of the flow. Gas and liquid are separated by gravity at the exit of the channel. The well in which the liquid flows when leaving the channel is designed for ensuring a stationary position of the liquid free surface under the channel exit.

Liquid flow rates q_l are measured by a mass flow meter (Micro motion®); gas flow rates q_g are controlled by a gas mass flow meter and mass flow controller (Brooks® model 5850E). Liquid flow rates range from 1 to 3 L/h and gas flow rates from 0.22 to 9 L/h. The associated superficial liquid and gas velocities are defined as $0.069 \le j_l = q_l/l^2 \le 0.208$ m/s and $0.015 \le j_g = q_g/l^2 \le 0.675$ m/s.

Fluids are air and deionized water (density: $\rho_l = 1000$ kg/m^3, dynamic viscosity: $\mu_l = 10^{-3}$ Pa s; surface tension: $\sigma = 73$ mN/m). Experiments are performed at 295 K and atmospheric pressure.

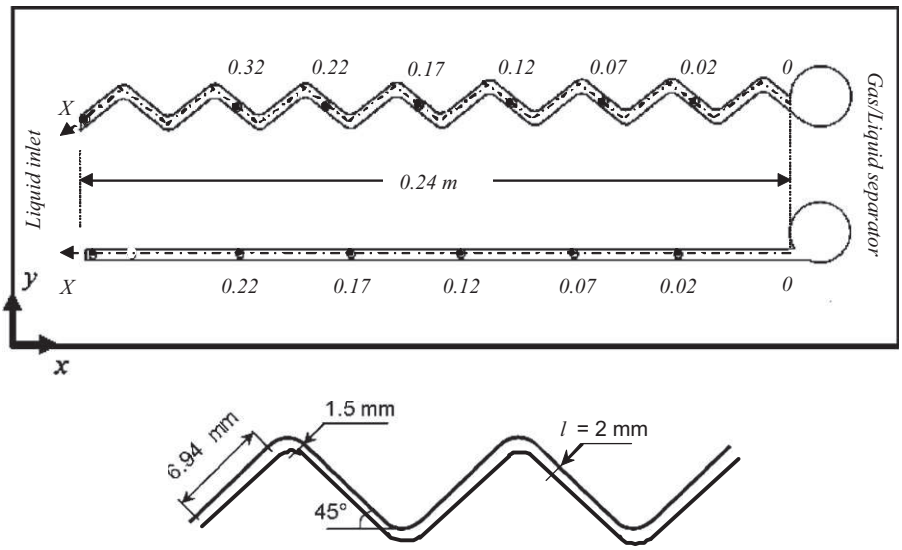

Fig. 1. Geometry of the straight and meandering channels (X corresponds to the location of the gas injection from the channel exit).

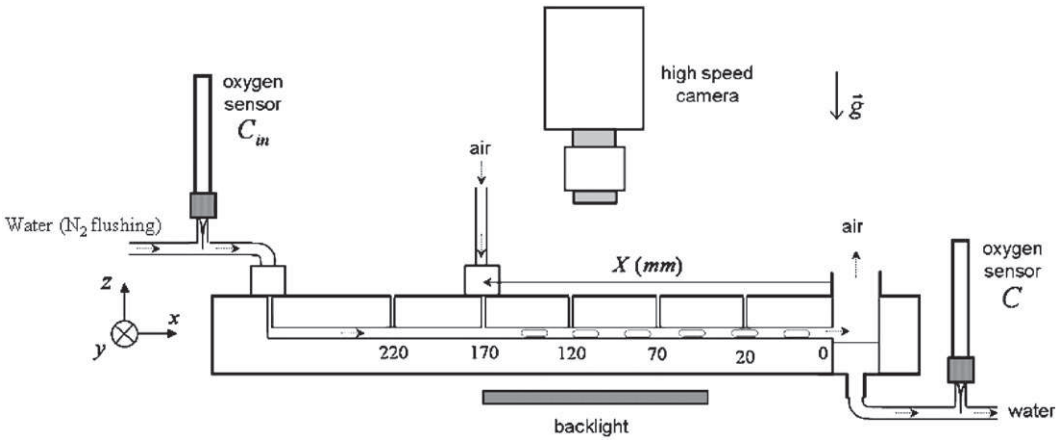

Fig. 2. Experimental set-up for gas–liquid mass transfer measurements.

2.2. Characterisation of gas–liquid flow hydrodynamics

The hydrodynamics of gas–liquid flows is investigated by a shadowgraph method. The channel is lit by a led backlight LitePad HO (Rosco®) while bubbles are filmed by means of a high-speed camera (NV1000) at 2000 frames per second (Fig. 2). Image resolution is 30 μm per pixel. The region of interest is 30 mm in length and 7.7 mm in width. A dedicated image analysis algorithm (developed using Matlab software®) is used to measure bubble length L_b, bubble velocity U and distance between the nose of two consecutive bubbles (called Unit Cell) L_{UC} (Fig. 3). Bubble velocity U is deduced, in the straight channel from average displacements of bubble nose between various time steps, and in the meandering channel from average times required by bubbles to flow along two bend periods. In the meandering channel, bubble and unit cell lengths are calculated from the sum of elementary segment lengths (two per bend) centred in the channel and intercepting the extremities of bubble. It is important to note that, whatever the channels, bubble characteristics (i.e. L_b, L_{UC}, U) have been determined, due to technical limitations, only in Taylor gas–liquid regime; indeed, these measurements impose to follow bubble displacements between two image acquisitions, and this is not possible when bubbles are too long ($L_b/l > 7$) or too fast. Using a larger measurement window would lead to significant accuracy losses (spatial resolution versus bubble size).

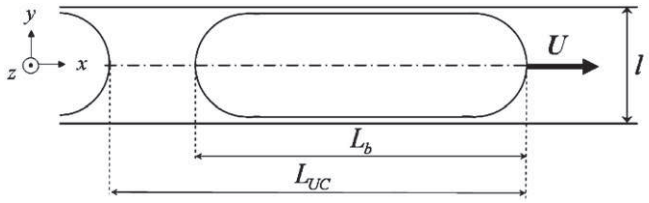

Fig. 3. Schematic representation of two consecutive bubbles inside the channel (Unit Cell).

For each injection position X, images of gas–liquid flow are recorded by camera, enabling thus eventual variations induced by a change in positions of gas injector to be quantified. For a given liquid and gas mass flow rates, the standard deviations of gas–liquid flow parameters (U, L_{UC} and L_b) between various injector positions have been found smaller than 4% of the averaged value.

2.3. Measurements of gas–liquid mass transfer

The transfer of oxygen from air bubbles into water is investigated in both channels and over the whole range of gas and liquid flow rates. For that, an original method is implemented, based on the use of two oxygen microsensors (Unisense® OX500, 400–600 μm in tip diameter) located a few centimetres before the entrance and after the exit of the channels. They are fixed, by

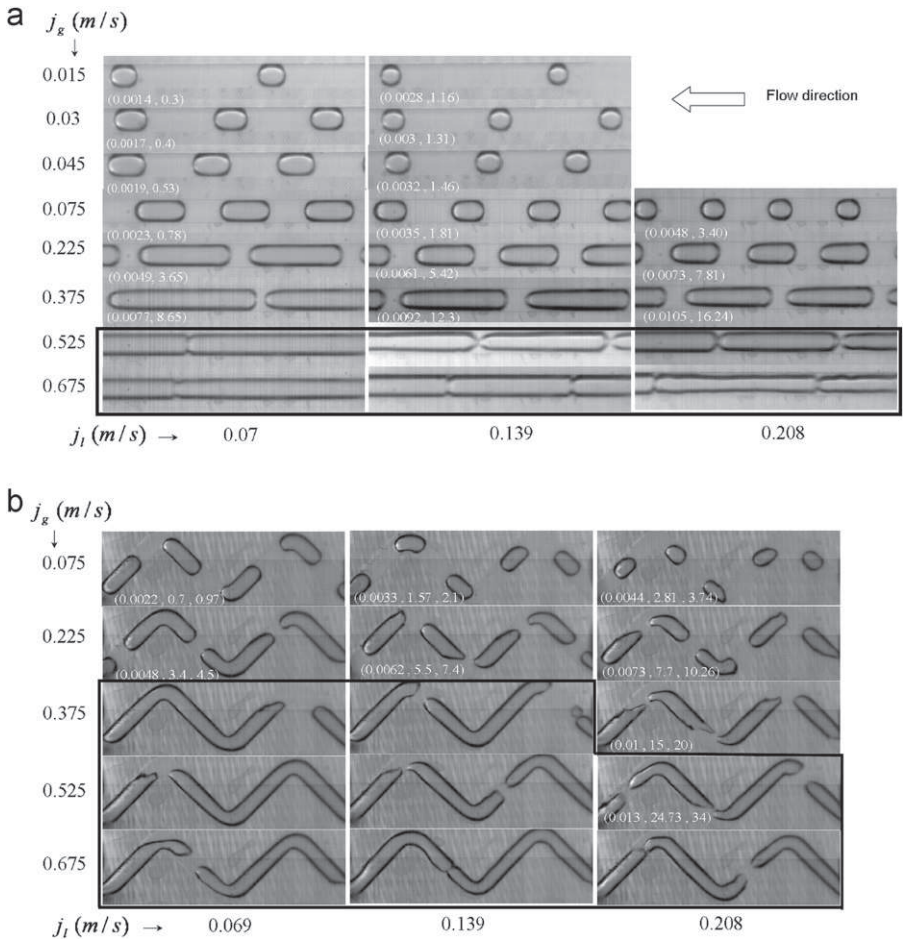

Fig. 4. Cartography of gas–liquid flows (in the horizontal plan Oxy defined in Fig. 3). Horizontal axis: liquid superficial velocity j_l. Vertical axis: gas superficial velocity j_g. The bubble moves from right to left. The Taylor and the slug-annular regimes correspond to the bubbles outside and inside the dark continuous line, respectively: (a) straight channel: white numbers correspond to (*Ca*, *We*) and (b) meandering channel. White numbers correspond to (*Ca*, *We*, *Ce*).

means of glass T-junctions, perpendicular to the tubing where the liquid phase flows. Coupled with an A/D-converter (Unisense® ADC216) and a versatile two-channel picoammeter (Unisense® PA2000), these microsensors then enable the difference of dissolved oxygen concentrations between channel entrance, C_{in}, and separator, C, to be measured (Fig. 2). Note that, as oxygen concentration at saturation, C^*, in deionised water at 295 K and atmospheric pressure is known (8.75 mg/L), the conversion of sensor signal from partial pressure to oxygen concentration can be easily calculated. The accuracy of the measurements is estimated to be within 0.01 mg/L.

Before the channel inlet, dissolved oxygen is removed from deionised water by bubbling nitrogen: whatever the gas–liquid flow rates, C_{in} is always kept smaller than $0.05C$. When bubble injection starts, the microsensor signal at the channel exit increases and quickly reaches a constant value which corresponds to concentration in dissolved oxygen noticed C. For the operating conditions tested, C remain smaller than 65% of equilibrium concentration of oxygen with ambient air C^*, showing that the present channel length is not sufficient to fully saturate the liquid phase in oxygen at the channel end.

As the microsensor is located after the separating well (3.1 cm^2), some precautions have been taken to minimise the bias induced by surface mass transfer occurring at this well; it involves nitrogen being blowing over the free surface. For more accuracy, the contribution of the separating well to total mass transfer has been quantified; for that, the values of $(C-C_{in})$ without bubbles in the channel and without blowing nitrogen above the well have been measured for different values of C_{in}. These experiments have revealed that, for $0.02C < C_{in} < 0.6C$, the ratio $(C-C_{in})/C_{in}$ is approximatively equal to 0.04: the contribution of free surface to total mass transfer is thus negligible.

3. Gas/liquid hydrodynamics

3.1. Flow regimes and bubble shape

Image cartographies of gas/liquid flow regimes are shown in Fig. 4a and b for the straight and meandering channels, respectively. For the present operating conditions ($1 \le q_l \le 3$ L h^{-1}, $0.2 \le q_g \le 9$ L h^{-1}), two regimes can be identified:

- the Taylor flow regime, where bubble lengths (L_b) and distances separating two consecutive bubbles ($L_{UC}-L_b$) are constant along the channel length.
- the slug-annular flow regime, where long bubbles break and coalesce.

In the straight channel, the bubble shape remains stable with time, whereas some periodic deformations of bubble ends are observed in the meandering channel due to centrifugal forces.

In Fig. 5, gas–liquid flow maps (i.e. superficial liquid velocity versus superficial gas velocity) are represented for each channel. They show that the transition from Taylor regime to slug-annular regime in the straight and meandering channels occurs for different superficial gas velocities. For the straight channel, this transition occurs at $0.38 \le j_g \le 0.51$ m/s in the range of the liquid flow rates investigated, whereas for the meandering channel, the transition occurs at $0.23 \le j_g \le 0.38$ m/s when $j_l \le 0.14$ m/s and at $0.51 \le j_g \le 0.68$ m/s when $j_l > 0.14$ m/s.

The shape of a bubble confined in a straight milli-channel depends on six parameters: ρ, μ, σ, g, l and U. According to the

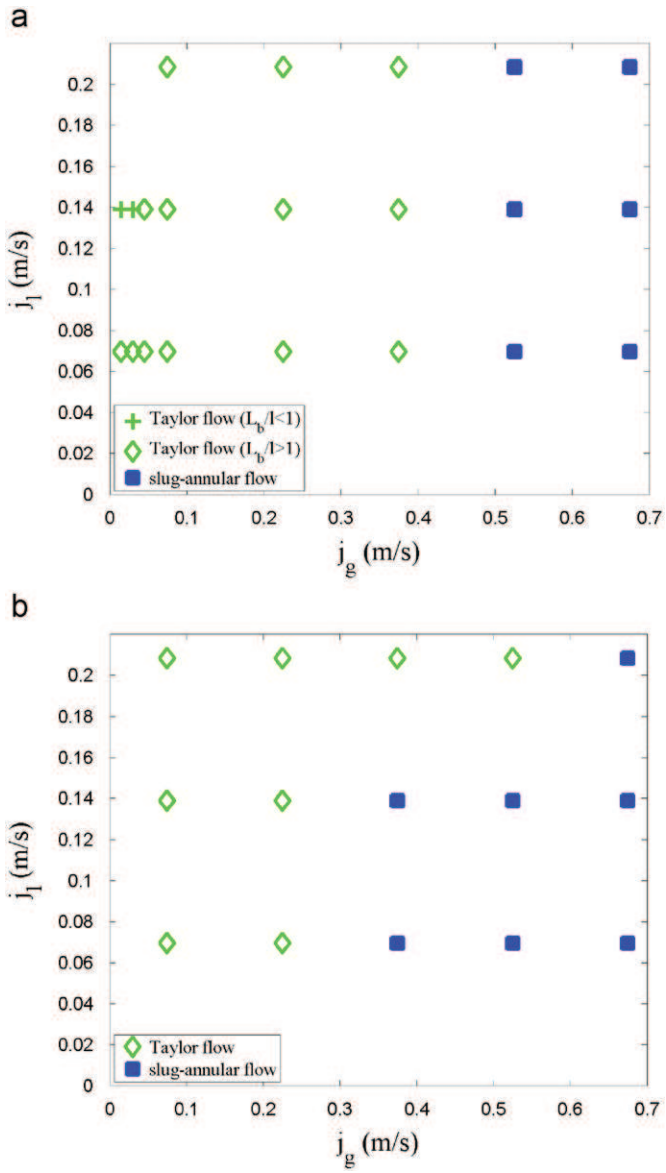

Fig. 5. Gas–liquid flow regime maps (liquid superficial velocity versus gas superficial velocity): Taylor flow $L_b/l < 1$ (+); Taylor flow $L_b/l > 1$ (◇); slug-annular flow (□). (a) straight channel and (b) meandering channel.

Buckingham π-theorem, the problem can therefore be solved using dimensional analysis, with three parameters:

- the capillary number:

$$Ca = \frac{\mu_l U}{\sigma} \tag{1}$$

- the Weber number

$$We = \frac{\rho_l U^2 l}{\sigma} \tag{2}$$

- the Bond number

$$Bo = \frac{\rho_l g l^2}{\sigma} \tag{3}$$

They compare, respectively, the effect of viscosity, inertia and gravity with capillary effects. For the meandering channel, the effect of centrifugal force due to bend curvature should also be

taken into account. The comparison between centrifugal forces and capillary effects is given by the dimensionless number:

$$Ce = \frac{\rho_L U^2 l^2}{\sigma r_c} \tag{4}$$

where r_c is the curvature radius of the bends. In Fig. 6, these dimensionless numbers are represented (only for the Taylor flow regime) as a function of the liquid Reynolds number,

$$Re = \frac{\rho_l U l}{\mu_l} = \frac{We}{Ca} \tag{5}$$

which compares inertial effects to viscous effects.

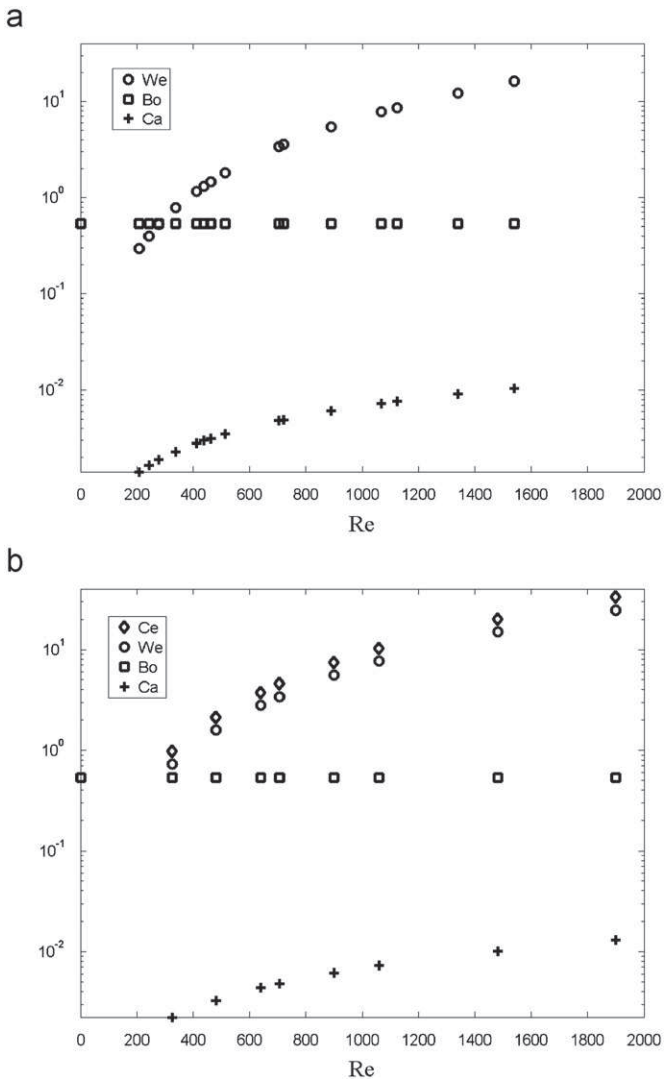

Fig. 6. Non-dimensional numbers controlling the bubble shape versus liquid Reynolds number (Taylor regime): (a) straight channel and (b) meandering channel.

The values of *Re* range from 200 to 1600, indicating that the inertial effects are important in the liquid phase. They also reveal that the inertial effects will largely contribute to the deformation of bubbles. In fact, the comparison of the numbers controlling the bubble shape reveals that inertial effects are dominant with respect to viscosity and gravity effects: Weber numbers *We* are higher than capillary numbers *Ca* and Bond number *Bo*, except for $Re < 250$ where inertial and gravity effects have the same order of magnitude. The cartography of bubble shape presented in Fig. 4 shows that, when increasing *Ca* and *We*, the bubble shape changes. For creeping flows, Giavedoni and Saita (1999) showed that the bubble shape is slightly deformed when $Ca < 0.01$. In the present case, as $0.001 < Ca < 0.01$, the significant variation of bubble shape cannot be thus attributed to viscous effects, but rather to inertial effects ($0.3 < We < 17$). Detailed observations of bubble changes in shape with *We* (Fig. 4a) demonstrate that for $We < 1.5$, the nose and the rear menisci are well described by two hemispheres whereas, for $We > 1.5$, the rear meniscus goes flat while the front meniscus becomes slender. This result is in agreement with the numerical works of Kreutzer et al. (2003) and Giavedoni and Saita (1999): indeed, for $Ca < 0.01$ and $We < 8$ ($Re < 200$), these authors observed the same variation in bubble shape as here. In the meandering channel, centrifugal forces have the same order of magnitude as inertial forces ($Ce \approx We$) (Fig. 6b), they will also contribute to deform the bubble shape in an asymmetric way in the curved region.

The effect of gravity has also been observed in the straight channel by filming bubbles in the vertical plane (Oxz). Fig. 7 shows how the bubble surface projected in a vertical plane is deformed asymmetrically. The Bond number is constant whatever the experimental conditions, and remains lower than one. The bubble deformations do not then result from the competition between gravity and surface tension forces, but rather from the fact that gravitational forces push the bubble against the top wall of the channel, and consequently that the inertial and viscous forces act differently on the top and bottom sides of the bubble. When increasing *We* and *Ca*, the bubble deformation becomes more pronounced.

3.2. Flow structure (Taylor regime)

In a frame of reference moving with bubbles, the streamlines of the liquid flow surrounding bubbles outline two distinct regions: a recirculating region and a liquid film region (Thulasidas et al., 1997; Taha and Cui, 2006; Kreutzer et al., 2005). This is schematically illustrated in Fig. 8. The film and recirculating regions can be defined by considering that a streamsurface connecting the stagnation points at the front and rear of the bubble surface separates them. Under this assumption, the liquid inside the recirculating region is like trapped between two consecutive bubbles and the average velocity of the recirculating region is equal to the bubble velocity.

As the flow is periodic with a period $T = L_{UC}/U$, the volume of liquid passing through a transversal section of the channel during T is

$$V_{l,circ} = q_l T \tag{6}$$

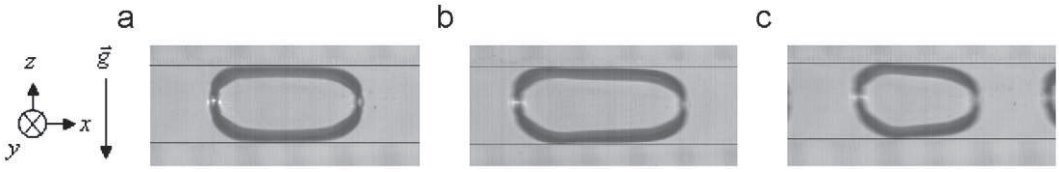

Fig. 7. Bubble in the vertical plan Oxz: (a) $Ca = 0.002$, $We = 0.54$; (b) $Ca = 0.006$, $We = 5.4$; and (c) $Ca = 0.0073$, $We = 7.8$.

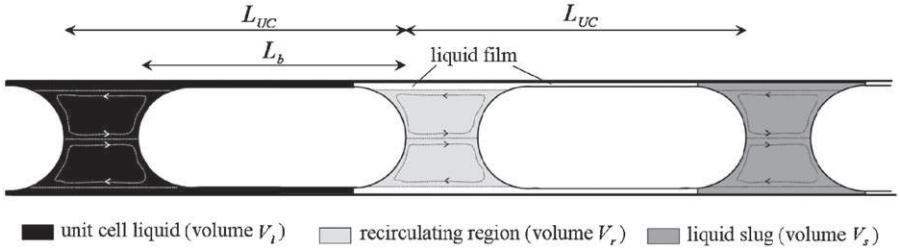

Fig. 8. Schematic representation of the liquid recirculation region and the liquid film region for bubbles in a horizontal Taylor flow regime.

and can be split into

$$V_{l,circ} = q_f T + V_r \tag{7}$$

where V_r is the volume of the liquid recirculating region and ($q_f T$) the contribution of the liquid film if q_f is the liquid flow rate in the film region. The volume of liquid recirculating region (V_r) depends on the location of the dividing streamsurface and on the distance between two consecutive bubbles ($L_{UC}-L_b$). According to Fries et al. (2008), for the present range of Capillary numbers ($0.001 < Ca < 0.01$), the variation of film thicknesses δ can be assumed negligible when compared to the channel width and the position of the dividing streamsurface constant ($0.10 < \delta/l < 0.18$ in the corner).

If no liquid flow is assumed in the film region ($q_f=0$), the liquid would be transported only inside the recirculating area and then $V_{l,circ}=V_r$ (Eq. (7)). In this case, the circulating volume $V_{l,circ}$ is linked to the characteristic volume of liquid trapped between two consecutives bubbles V_s (called liquid slug volume) and is geometrically defined in Fig. 8. Assuming that, *in the Taylor regime*, the ends of the bubbles are hemispherical (with a diameter equal to l), the liquid slug volume V_s is given by:

$$V_s = A(L_{UC}-L_b) + l^3\left(1-\frac{\pi}{6}\right) \tag{8}$$

where A is the channel cross-sectional area. For the straight channel, Fig. 9a compares the two liquid volumes, $V_{l,circ}$ (Eq. (7) with $q_f=0$) and V_s (Eq. (8)), when varying relative slug lengths $(L_{UC}-L_b)/L_{UC}$. Note that low values of $(L_{UC}-L_b)/L_{UC}$ correspond to long bubbles and short liquid slugs, while $(L_{UC}-L_b)/L_{UC} \cong 1$ correspond to long liquid slugs and short bubbles. This figure shows that $V_{l,circ}$ is proportional to $V_s$whatever the slug lengths (in the Taylor regime):

$$V_{l,circ} \cong 0.74 V_s \tag{9}$$

Such finding indicates that the main part of the liquid phase is transported inside the recirculating area. As a consequence, in the present experiments, the contribution of liquid film to liquid transport along the channel length can be neglected and the liquid film reasonably considered as stagnant. This is explained by the presence of an important dead volume of liquid in the corners of the channel: Fries et al. (2008) estimated that, for $2.10^{-4} < Ca < 10^{-2}$, the liquid in channel corners represents about 70% of the total film area. Note that for the meandering channel, Eq. (8) is not relevant for calculating the slug volume because of large deformations of bubble ends, and so the ratio $V_{l,circ}/V_s$ cannot be calculated.

For the straight channel, Fig. 9b compares the circulating volume ($V_{l,circ}$) to the liquid volume in a unit cell (V_l) when varying the relative slug length$(L_{UC}-L_b)/L_{UC}$. The volume V_l is deduced from the difference between the total volume of the unit cell and the bubble volume V_b. According to the periodicity of the flow, it leads to

$$V_b = q_g T \tag{10}$$

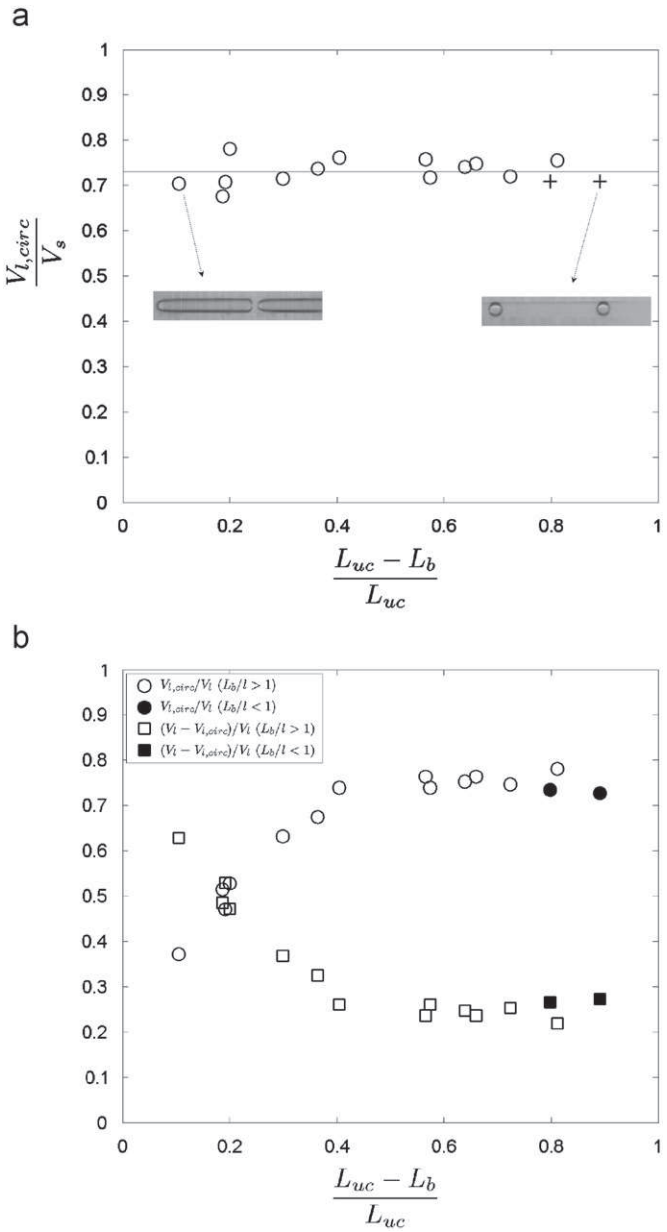

Fig. 9. Comparison, as a function of relative slug lengths, between the liquid volume crossing a transversal section of the channel during a period T ($V_{l,circ}$) and: (a) the liquid slug volume (V_s) [$L_b/l<1$: +; $L_b/l>1$: ○]; (b) the liquid volume in a unit cell (V_l) [$V_{l,circ}/V_l$: ○; $(V_l-V_{l,circ})/V_l$: □; Dark symbols correspond to $L_b/L_{UC} \leq 1$]; This comparison is restricted to the straight channel and the Taylor regime.

and so,

$$V_l = L_{UC}A - q_g T \tag{11}$$

For$(L_{UC}-L_b)/L_{UC}>0.5$ (short bubbles and long liquid slugs), the ratio $V_{l,circ}/V_l$ is constant and equal to 0.74. This is a consequence at the fact that the volume of liquid film in contact with the bubble is negligible when compared to liquid slug volume (Fig. 9a). Thus, $V_l \cong V_s$ and Eq. (9) gives $V_{l,circ}/V_l \cong 0.74$. The liquid film being assumed stagnant, this value can be analysed as an estimation of the relative cross-sectional area of the liquid recirculating region.

When decreasing circulating volumes (i.e. increasing bubble lengths), the dead volume of liquid film is no longer negligible, and $V_{l,circ}/V_l$ decreases. The fraction of stagnant liquid film $(V_l-V_{l,circ})/V_l$ is also plotted in Fig. 9b. It is interesting to observe that: (i) for long liquid slug and short bubbles, the dead liquid volume represents about 26% of the total volume of liquid inside the channel, (ii) this fraction increases when decreasing the circulating volume V_l, until reaching more than 50% of the liquid of the unit cell volume for the smallest liquid slugs.

3.3. Bubble length (Taylor regime)

In the Taylor regime, Fig. 10a and b compare, for straight and meandering channels, the variation of bubble length (L_b) and slug length ($L_{UC}-L_b$) with superficial gas velocity (j_g), respectively. As expected, whatever the channels, bubble lengths increase for increasing gas and decreasing liquid superficial velocities, respectively; the smallest and largest bubbles are almost 1.8 and 12 mm in lengths respectively, leading to aspect ratio L_b/l of 0.88 to 6. Slug lengths ($L_{UC}-L_b$) significantly rise for decreasing gas velocities (almost from 1.4 to 15 mm, i.e. $0.7<(L_{UC}-L_b)/l<7$), but remain slightly dependent on liquid velocities. It can be noted that, for the present operating conditions, the Taylor regimes can be split into two sub-regimes:

- confined bubbles where $L_b/l>1$(the most encountered),
- unconfined bubbles where $L_b/l\leq 1$.

Generally, using a meandering channel instead of a straight channel enables a slight rise in bubble lengths (especially for the highest gas superficial velocities) while conserving almost identical slug lengths. This can be explained by the strong stretching of bubble ends when they move along the various bends of the meandering channel. Fig. 4b clearly illustrates this phenomenon.

For gas–liquid microfluidic flows, various dimensionless relationships are encountered in literature to correlate, from experimental data, bubble lengths with operating parameters, fluid properties, inlet conditions and channel characteristics (Garstecki et al., 2006; Van Steijn et al., 2007; Zhao and Middelberg, 2010). Even if most of them are based on the use of the ratio of gas superficial velocity with the liquid superficial velocity (j_g/j_l), the formulation of the correlation changes depending on channel shape (cross-sectional area, geometry), gas injection type (flow-focusing, T-junction) and characteristics (size and angle between main and secondary channels). Empirical coefficients are then determined to fit experimental data with the law chosen. In parallel to experimental works, numerical simulations of bubble formation are done to improve these modelling, and in particular to better understand the bubble formation dynamics and mechanism in microchannels (Jensen et al., 2005; Annaland et al., 2006; Qian and Lawal, 2006; Weber and Shandas, 2007; Goel and Buwa, 2009; Sobieszuk et al., 2010). In the present case, the following relationships have been applied:

$$\frac{L_b}{l}=a\left(\frac{j_g}{j_l}\right)^b \tag{12}$$

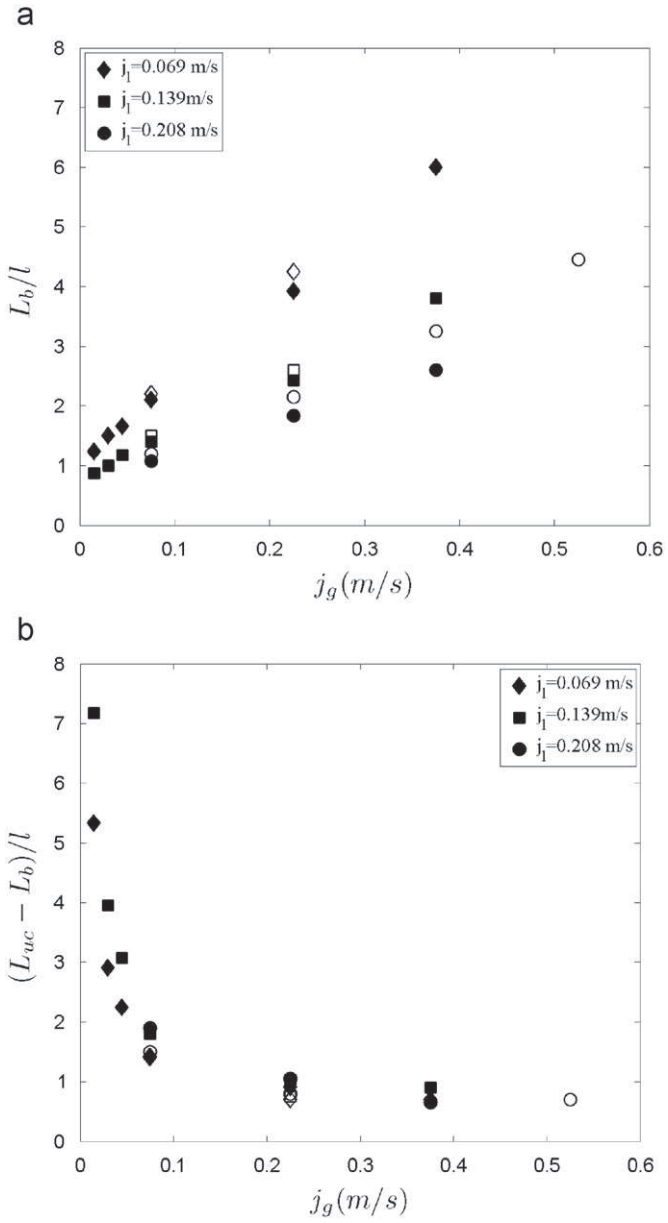

Fig. 10. Taylor regime: (a) bubble length (L_b) and (b) slug length ($L_{UC}-L_b$) versus superficial gas velocity for j_l=0.069 m/s (♦), j_l=0.139 m/s (■) and j_l=0.208 m/s (▲) [dark and white symbols correspond to straight and meandering channels, respectively].

$$\frac{L_b}{l}=a'\left(\frac{j_g}{j_l}\right)^{b'}Ca^{c'} \tag{13}$$

$$\frac{L_b}{l}=1+\alpha_2'\left(\frac{j_g}{j_l}\right) \tag{14}$$

$$\frac{L_b}{l}=\alpha_1+\alpha_2\left(\frac{j_g}{j_l}\right) \tag{15}$$

The associated coefficients are reported in Table 1. For the straight channel, Eq. (12) does not allow to predict with accuracy the confined bubble lengths having $L_b/l>3$, whereas, for the meandering channel, Eqs. (12) and (13) are equal ($c'=0$). The empirical coefficients b' and c' found in the straight channel have the same order of magnitude as those of Tan et al. (2009) (respectively, 0.5 and -0.2). For the meandering channel, the Capillary number has no effect on bubble length and the impact of the ratio j_g/j_l is slightly stronger than in the straight channel (b' is

Table 1
Modelling of bubble lengths: empirical coefficients associated with Eqs. (12)–(15).

	$\frac{L_b}{l}=a\left(\frac{j_g}{j_l}\right)^b$ (Eq. (12))			$\frac{L_b}{l}=a'\left(\frac{j_g}{j_l}\right)^{b'}Ca^{c'}$ (Eq. (13))			
	a	b	std (%)	a'	b'	c'	std (%)
Straight channel	1.93	0.43	11.5	1.12	0.54	−0.12	9
Meandering channel	2.15	0.58	6	2.15	0.58	0	6
	$\frac{L_b}{l}=1+\alpha_2\left(\frac{j_g}{j_l}\right)$ (Eq. (14))			$\frac{L_b}{l}=\alpha_1+\alpha_2\left(\frac{j_g}{j_l}\right)$ (Eq. (15))			
	α_2	std (%)		α_1		α_2	std (%)
Straight channel	0.93	8.7		0.91		0.96	7.1
Meandering channel	1.13	8.4		0.90		1.17	6.7

equal to 0.58 instead of 0.54, respectively). Garstecki et al. (2006) and Van Steijn et al. (2007) established, respectively, Eqs. (14) and (15) from a mechanistic approach of bubble formation dynamics. For small capillary numbers, they demonstrated that the dominant effect in the break-up of either liquid or gaseous streams in the continuous fluid is the balance of hydrostatic pressures in the two immiscible fluids. The 'squeezing' mechanism of break-up is specific to microsystems as it depends crucially on the blockage of the channel by a liquid or gaseous plug. This mechanism allows these authors to formulate simple scaling laws that predict the size of droplets and bubbles produced in microfluidic T-junctions from only the ratio between dispersed and continuous flow rates. As shown in Table 1, the first coefficient α_1 is almost equal for both channels and close to one as predicted by Garstecki et al. (2006). On the contrary, the second coefficients, α_2 and α_2', are higher for the meandering channel than for the straight channel while remaining also close to the unity.

Pohorecki and Kula (2008) have described a simple "switching" mechanism to explain the form of the CFD-based correlation proposed by Qian and Lawal (2006) in which the length of gas bubble is inversely proportional to the liquid hold-up, $\varepsilon_l=j_l/(j_l+j_g)$. This type of relationship is fully verified in the case of the present data (standard deviation below 8%): it leads to proportionality coefficients equal to 1.76 and to 2.00 in the straight and meandering channels, respectively (a value of 1.637 was reported by Qian and Lawal, 2006). Note that, recently, corrected values of the pre-exponent constant and the exponents in the Qian and Lawal (2006) correlation have been suggested by Sobieszuk et al. (2010) (respectively, 1.3, 0.07 for $\varepsilon_g=j_g/(j_l+j_g)$, −1.01 for $\varepsilon_l=j_l/(j_l+j_g)$ and −0.1 for Weber number). When applying such coefficients to the present case, experimental bubble lengths are overestimated by 30%.

3.4. Bubble velocity (Taylor regime)

In Fig. 11a, the bubble velocity U is plotted, in the Taylor regime, as a function of the total superficial velocity j defined as

$$j=j_g+j_l \tag{16}$$

Whatever the channels, the bubble velocity is always larger than the superficial velocity, demonstrating thus that bubbles travel faster than the sum of gas and liquid superficial velocities, or in other words, that a slip phenomenon between bubbles and liquid flow takes place. The bubble velocity can be successfully related to the total velocity according to an affine function. The proportionality coefficient, usually noted C_0, is found equal to 1.27 and to 1.25 for the straight and meandering channels, respectively. These latter values are in agreement with the ones found by Laborie et al. (1999) in millimetric capillaries (1.24 for water at 25 °C).

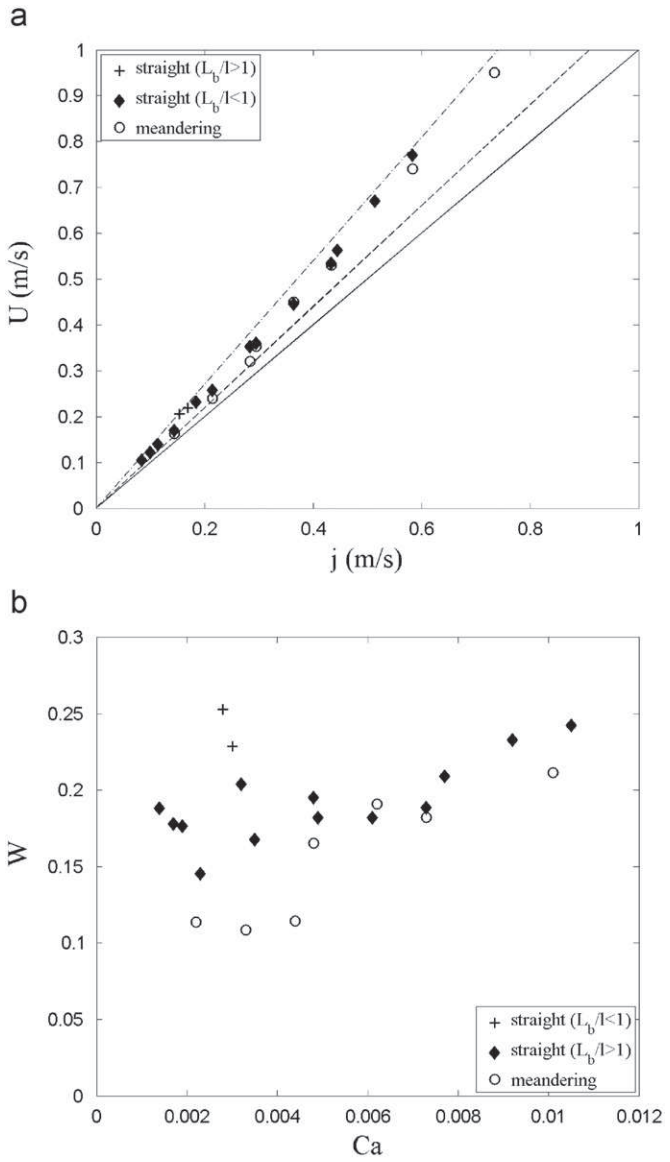

Fig. 11. (a) Bubble velocity versus superficial velocity The continuous line corresponds to $U=j$, the dotted line (–) to $U=1.1j$, and the dotted line with points (· – · –) to $U=1.35j$ (Taylor flow regime with $L_b<l$: +) and (b) relative slip velocity versus capillary number (Taylor flow regime with $L_b<l$: +).

Assuming incompressible fluids, the mass balance equation for gas and liquid phase gives

$$A_bU=Aj-q_f \tag{17}$$

where A_b is the bubble cross-sectional area, A the channel cross-sectional area and q_f the liquid flow rate in the film between channel walls and bubbles. Details about the development leading to Eq. (17) are given by Thulasidas et al. (1995). The relative slip velocity is expressed by

$$W = \frac{U-j}{U} \tag{18}$$

The introduction of Eq. (18) into Eq. (17) leads to

$$W = \frac{A_f}{A} - \frac{q_f}{AU} \tag{19}$$

where A_f is the cross-sectional area of the liquid film ($A_f = A - A_b$).

The variation of W with Ca is reported in Fig. 11b. For confined bubbles ($L_b > l$) moving in the straight channel, W slightly increases from 0.17 to 0.25 with increasing Ca. Highest W (i.e. 0.23–0.25) are observed for $L_b < l$. As the liquid film can reasonably be considered as stagnant ($q_f = 0$), the values of W provide an estimation of the relative cross-sectional area of the liquid film. The increase of liquid film due to a decrease of the bubble size from $L_b > l$ to $L_b < l$ is thus responsible for the highest values of W. In the meandering channel, the same tendencies can be observed even if, for $Ca < 0.006$, the associated slip velocities W remain smaller than the ones in the straight channel. Because of the complex flow induced by the bends, no reliable assumption can be emitted at present with respect to the liquid film: deeper investigations are required to fully understand this trend.

4. Mass transfer

4.1. Volumetric mass transfer coefficients

4.1.1. Theoretical developments

As the flow is periodic, the flux of oxygen living the channel, $F(X,t)$, is also periodic. Thus, the averaged flux of oxygen over a period, defined by Eq. (20), is constant:

$$\overline{F}(X) = \frac{1}{T}\int_0^T F(X,t)\,dt \tag{20}$$

As the liquid phase is well mixed inside the separator and the concentration recorded by the oxygen microsensor $C(X)$ constant in time, the averaged oxygen flux is given by

$$\overline{F}(X) = q_l C(X) \tag{21}$$

The variations of concentrations in dissolved oxygen at the exit of the channel, C, with the length of gas–liquid flow, X, are illustrated in Fig. 12 for different flow rates. This figure shows that C increases with increasing X. Reminding that X corresponds to the location of gas injection from the channel outlet (Fig. 2), the increase of $C(X)$ is then caused by the increase of contact times between both phases. It can be observed that, when a fitting of the experimental values of C with X is applied (taking the concentration at $X=0.2$ as reference), different values are obtained at $X=0$: this is due to the fact that some mass transfer occurs during the bubble formation time.

As the flow characteristics (U, L_{UC} and L_b) are independent of gas injection locations X, the variation of the flux with X provides the volumetric mass flux of oxygen from gas to liquid along the channel, such as

$$\varphi(X) = \frac{1}{A}\frac{d\overline{F}}{dX} \tag{22}$$

Eqs. (21) and (22) leads then to

$$\varphi(X) = j_l \frac{dC}{dX} \tag{23}$$

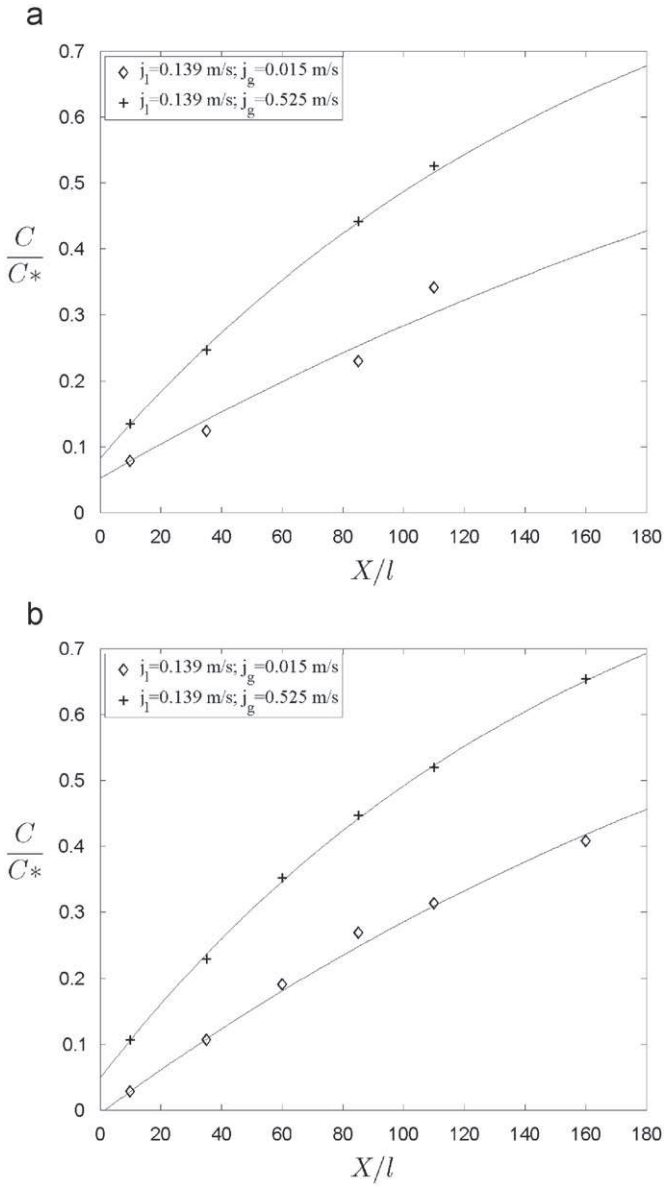

Fig. 12. Oxygen concentration at the exit of the channel C (normalised by saturation concentration C^*) versus length of gas–liquid flow X (normalised by channel size l) for $j_l = 0.139$ m/s and two gas superficial velocities ($j_g = 0.015$ m/s: □; $j_g = 0.525$ m/s: +). $X=0$ corresponds to the channel exit (Fig. 2) and the continuous line results from the fitting of the experiment values by Eq. (28): (a) straight channel and (b) meandering channel.

Assuming an uniform concentration of oxygen in liquid at the scale of the unit cell, then the volumetric flux of oxygen can be expressed by

$$\varphi(X) = K_l a(C^* - C(X)) \tag{24}$$

where K_l is the overall mass transfer coefficient in the liquid side and a the interfacial area between gas and liquid phases. The double film theory of Lewis and Whitman (1924) assumes that the overall mass transfer coefficient K_l is the result of two local mass transfer coefficients (k_l and k_g):

$$\frac{1}{K_l} = \frac{1}{k_l} + \frac{1}{mk_g} \tag{25}$$

where m is linked to the Henry's constant ($m = H/P$). As the solubility of oxygen in deionised water is low ($m = 39{,}950$ at 293 K), all the resistance to oxygen mass transfer is located in the

liquid film, leading to

$$\frac{1}{K_l} \approx \frac{1}{k_l} \tag{26}$$

So, by coupling Eqs. (23), (24) and (26), the usual relationship based on a plug flow model in liquid phase is found:

$$\frac{dC}{dX} = \frac{k_l a}{j_l}(C^* - C(X)) \tag{27}$$

As the initial oxygen concentration in the liquid phase (C_{in}) is null (nitrogen flushing), the integration of Eq. (27) gives

$$\frac{C}{C^*} = 1 - \exp\left(-\frac{k_l a}{j_l} X\right) \tag{28}$$

By applying the experimental values of C/C^* to the latter equation, volumetric mass transfer coefficients, $k_l a$, can be determined. Note that this fitting has been obtained with satisfaction (i.e. with a mean standard deviation below 10%) for all the experimental concentration profiles except for the ones corresponding to unconfined bubbles ($L_b < l$). This could be explained by the fact that, for confined bubbles, the liquid inside the recirculating region between two consecutive bubbles is well mixed, and the oxygen concentration C can be reasonably assumed uniform; in these conditions, the driving force for mass transfer at a gas–liquid interface is well described by $C^* - C$. On the contrary, the transition from confined to unconfined bubble flows induces a disappearance of liquid recirculating loops in the region between two consecutive bubbles, implying thus that the assumption of a uniform concentration C is no longer verified and Eq. (27) becomes invalid.

4.1.2. Results

The variation of $k_l a$ with gas superficial velocity is plotted in Fig. 13 for the Taylor ($L_b > l$) and slug-annular regimes.

For the straight channel (Fig. 13a), it can be observed that: (i) for a given value of j_g, $k_l a$ increases with increasing j_l, (ii) for a fixed value of j_l, $k_l a$ increases when increasing j_g until reaching a maximum and then decreases. A rise of j_l above 0.139 m/s has no significant effect on $k_l a$. The flow regimes reported in Fig. 13a (empty and dark symbols) show that the decrease of $k_l a$ when increasing j_g above 0.4 m/s coincides with the transition from Taylor regime to slug-annular regime. These trends (i.e. parabolic variation of $k_l a$ with j_g) are in agreement with the results reported in the literature involving chemical or physical methods (for example, absorption of pure CO_2 in water or in sodium hydroxide solutions), either in rectangular microchannels (Yue et al., 2007) or in circular millichannels (Tortopidis and Bontozoglou, 1997; Bercic and Pintar, 1997; Vandu et al., 2005).

For the meandering channel (Fig. 13b), the variation of $k_l a$ with both superficial velocities look identical to the ones with the straight channel, except that the values of $k_l a$ remain almost constant after a critical gas superficial velocity. This latter parameter depends on the liquid superficial velocity. Here also, this is directly correlated to the regime transition.

The comparison of both channels (Fig. 13a and b) shows that, in the Taylor flow regime ($j_g < 0.4$ m/s), at a given couple (j_g, j_l), $k_l a$ are only slightly higher in the meandering channel than in the straight one; this would suggest that the changes in gas–liquid hydrodynamic induced by the bends have no major positive consequence on mass transfer in the Taylor flow regime. On the contrary, in the slug-annular regime, using a meandering channel enables to increase significantly volumetric mass transfer coefficients. Thus, the meandering channel appears more competitive than the straight channel mainly at high gas flow rates; the main reason should be the delay of the regime transition induced by the bends.

At last, it is interesting to compare these results with the volumetric mass transfer coefficients obtained with usual gas–liquid contactors. As shown in Fig. 13, using millimetric channels (with a sufficient gas superficial velocity, i.e. $j_G > 0.2$–0.3 m/s) enable some values of $k_l a$ varying between 0.2 and 0.65 s^{-1} to be reached in a water/air system (Fig. 13): they are logically higher than in bubble columns ($0.005 < k_l a < 0.24\ s^{-1}$) or in stirred tanks ($0.03 < k_l a < 0.4\ s^{-1}$), but remain with the same order of magnitude as in static mixers ($0.1 < k_l a < 2.5\ s^{-1}$) and smaller than in microchannels ($0.3 < k_l a < 21\ s^{-1}$) (Yue et al., 2007). Thus, gas–liquid millimetric channel contactors represent a promising compromise for intensifying mass transfer performances while involving controlled gas–liquid flows with low power inputs (contrary to static mixers) and while working at sufficient flow rates for industrial processes (L h^{-1} against mL min^{-1} in microreactors).

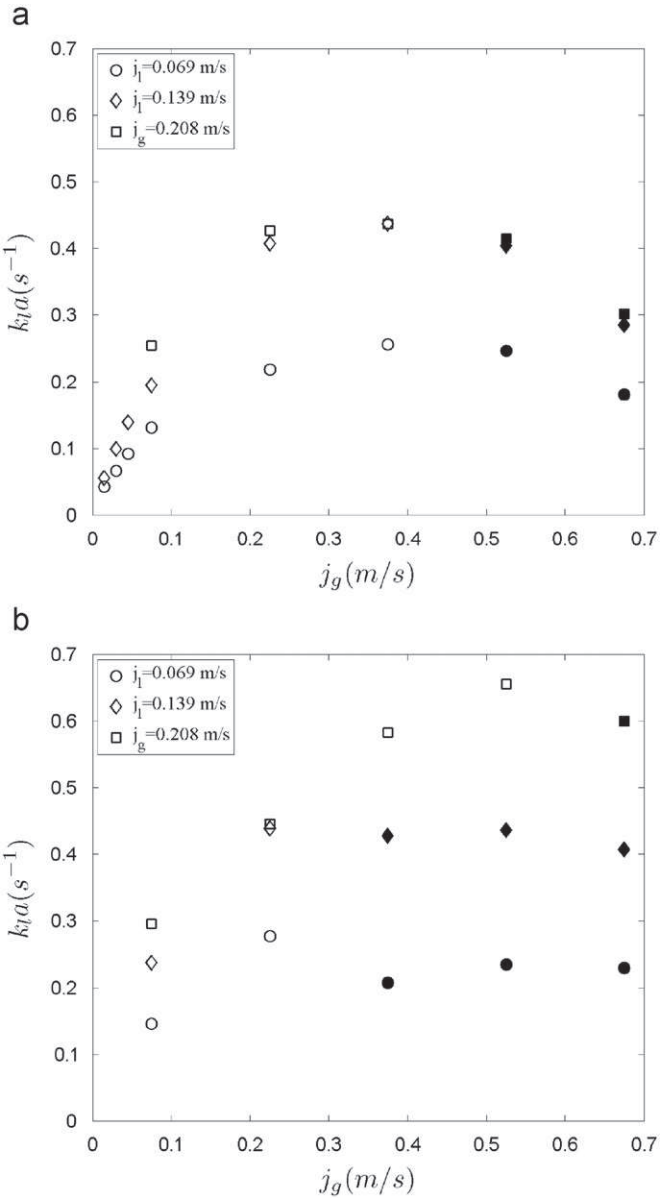

Fig. 13. Volumetric mass transfer coefficient versus gas superficial velocity for j_l=0.069 m/s (○), j_l=0.139 m/s (◇) and j_l=0.208 m/s (□). White and dark symbols correspond to the Taylor flow ($L_b > l$) and the slug-annular flow regimes, respectively. (a) Straight channel and (b) meandering channel.

4.2. Mass transfer efficiency

One method for sizing macro-scale gas–liquid contactors consists in using the concepts of Number of Transfer Units

(*NTU*) and Height of Transfer Units (*HTU*), defined such as

$$Z = NTU_g \times HTU_g = NTU_l \times HTU_l \tag{29}$$

where Z is the height of gas–liquid contactor. For liquid phase, NTU_l and HTU_l are expressed as

$$NTU_l = \int_{x_{mol,in}}^{x_{mol,ex}} \frac{dx_{mol}}{(x^*_{mol} - x_{mol})(1 - x_{mol})} \tag{30}$$

$$HTU_l = \frac{L}{K_l^0 a^0 \Omega} \tag{31}$$

where x_{mol} is the molar fraction in the liquid phase of the transferring compound, L the molar liquid flow rate, K_l^0 the overall liquid mass transfer coefficient, with units, $\mathrm{mol\,m^{-2}\,s^{-1}}$, a^0 the interfacial area defined per reactor volume unit, and Ω the cross-sectional area of gas–liquid contactor. The combination of Eqs. (29) and (31) leads to

$$NTU_l = \frac{Z}{HTU_L} = \frac{ZK_l^0 a^0 \Omega}{L} \tag{32}$$

If K_l^0 is converted into K_l (expressed in m/s) and L into volumetric liquid flow rate (q_l), Eq. (32) becomes when $K_l \approx k_l$ (Eq. (26)):

$$NTU_l = \frac{V/q_l}{1/(k_l a)} = \frac{\tau}{t_{transfer}} \tag{33}$$

Then, we find again here the well-known alternative definition of NTU_l, that is to say the ratio between residence time of liquid phase (τ) and characteristic mass transfer time ($t_{transfer}$).

It is interesting to observe that, in the mass balance established in the present channels (Eq. (28)), the ratio included in the exponential function is nothing other than this NTU_l. with a residence time expressed as

$$\tau = \frac{V}{q_l} = \frac{l^2 X}{q_l} = \frac{X}{j_l} \tag{34}$$

and X is the location of the gas injection ($X=0$ at the exit). As already shown in Fig. 1, both channels have the same compactness in length (0.24 m), but the meandering channel has a higher developed straight length (0.34 m) due to the bends, than the straight channel (0.24 m). To calculate NTU_l, the maximal position X has been considered, i.e. $X=0.22$ and 0.32 m for the straight and meandering channels, respectively. In Fig. 14a, the variation of NTU_l with gas superficial velocity is plotted for each channel. For each channel, the Numbers of Transfer Units in the liquid phase are below 1.1, thus demonstrating that, in the present millimetric channels, residence times are smaller than mass transfer times, contrary to what is commonly observed for macro-scale processes. This clearly outlines that, even if millimetric channels allow gas–liquid mass transfer intensification (high $k_l a$), special attention should be paid for generating sufficient residence times. Fig. 14a also reveals that the meandering channel induces a higher Number of Transfer Units in the liquid phase than in the straight channel. This is the consequences of the fact that, in the meandering channel, the residence times τ are higher (Eq. (34) where X is 0.32 m against 0.22 m for the straight channel) as well as volumetric mass transfer coefficients $k_l a$ (especially in the slug-annular regimes for $j_g > 0.4$ m/s, Fig. 13).

For co-current absorption macro-scale processes, the Number of Transfer Units in the liquid phase is usually expressed, assuming plug-flows for both liquid and gas phases, as a function of the absorption ratio r and liquid efficiency E, according to (Roustan, 2003)

$$NTU_l = \frac{1}{r+1} \ln \frac{1}{1 - E(1+r)} \tag{35}$$

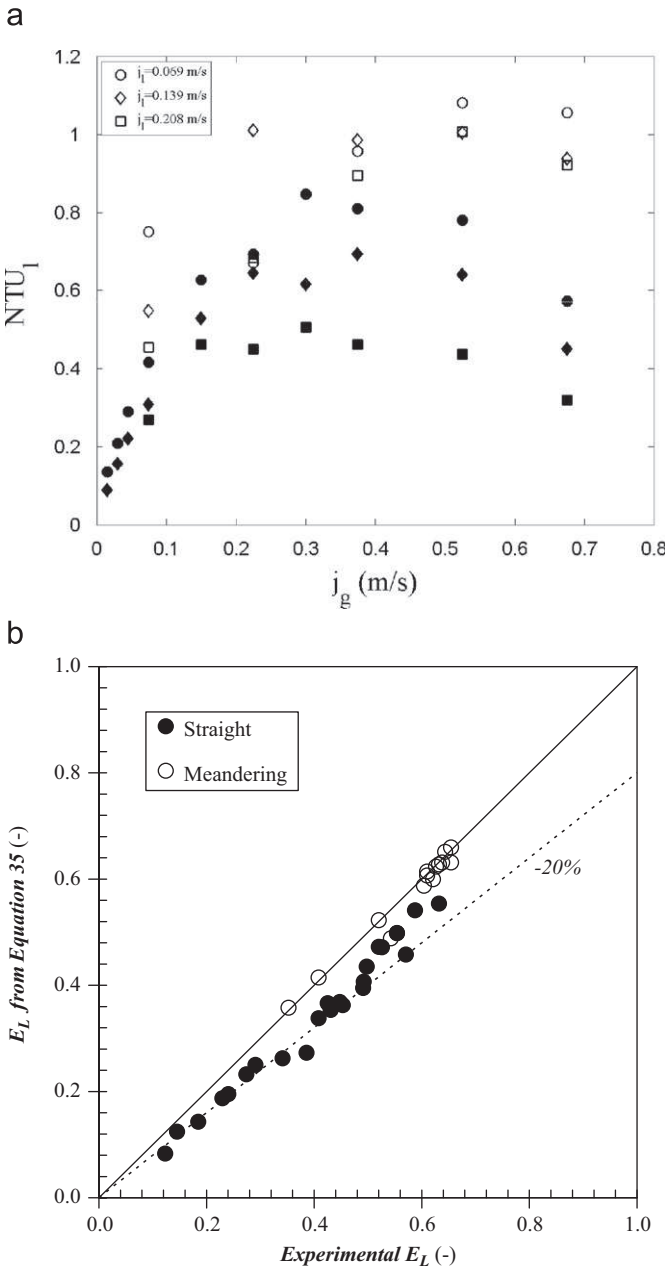

Fig. 14. (a) Number of Transfer Units in the liquid phase versus gas superficial velocity [Dark and Empty symbols correspond to the straight and meandering channels, respectively]: $j_l=0.069$ m/s (○), $j_l=0.139$ m/s (◇) and $j_l=0.208$ m/s (□). (b) Comparison between liquid absorption efficiencies measured and the ones calculated from Eq. (35).

with

$$r = \frac{L}{Gm} \tag{36}$$

L and G are the molar liquid and gas flow rates, respectively, and m the Henry'constant (Eq. (23), $m=39{,}950$ at 293 K). The Murphree efficiency in the liquid phase is written as

$$E = \frac{x_{mol,ex} - x_{mol,in}}{x^*_{mol} - x_{mol,in}} \tag{37}$$

where x_{mol} is the molar fraction of dissolved oxygen. Using concentrations instead of molar fractions and considering the

oxygen concentration at the inlet C_{in} equal to 0, Eq. (37) becomes

$$E = \frac{C}{C^*} \tag{38}$$

Knowing NTU_l (Fig. 14a) and deducing absorption ratio r from volumetric gas and liquid flow rates, liquid absorption efficiency E can be calculated from Eq. (35). They are compared in Fig. 14b with experimental values issued from Fig. 12. A good agreement between both efficiencies is obtained, which is quite logical insofar as when $r \to 0$ ($m \to \infty$), Eq. (35) becomes

$$NTU_l \approx \ln(1-E) \tag{39}$$

which is equivalent to

$$E = 1-\exp(-NTU_l) \tag{40}$$

So, when m is high (low solubility of transferring compound), Eq. (35) becomes strictly equivalent to the mass balance previously established for millimetric channels (Eq. (28)) under plug-flow assumption. The difference observed between both efficiencies can thus be attributed to the fact that, in Eq. (26), the resistance to mass transfer in the gas phase is considered null. These latter basic calculations confirm that the usual macro-scale law for gas–liquid absorption (Eq. (35)) remains applicable in millimetric channels.

The intensification of mass transfer in millimetric channels requires both to increase volumetric mass transfer coefficients (k_la) and the Number of Transfer Units in the liquid phase NTU_l (and consequently liquid absorption efficiency E). For given channel geometry (cross-sectional area $l \times l$, gas injection mode, material) and operating conditions (j_l, j_g, water/air, temperature pressure), volumetric mass transfer coefficients (and thus the transfer times) are fixed, and thus independent of the channel length X (provided that the effect of pressure drop on mass transfer remains negligible), whereas residence times τ are controlled by liquid flow rate and channel length (Eq. (34)). Thus, one simple way to increase NTU_l is to play on the channel length X. Using Eqs. (34)–(35) and (38), the length of channel required to reach a liquid absorption efficiency of 95% ($X_{E=0.95}$) can be estimated: Fig. 15 reports the variation of $X_{E=0.95}$ as a function of gas superficial velocity, at different j_l and for both channels. For the straight channel, whatever the liquid superficial velocity, $X_{E=0.95}$ is minimal at about $j_g \cong 0.4$ m/s (Fig. 15a) which corresponds to maximal values of k_la (Fig. 13a). For the meandering channel (Fig. 15b), $X_{E=0.95}$ decreases with increasing j_g until $j_g \approx 0.4$ m/s; above this value, $X_{E=0.95}$ becomes independent of j_g and j_l. The comparison of both Fig. 15a and b reveals that:

- for $j_g < 0.2$ m/s (unconfined bubbles and confined bubbles with $L_b/l \leq 3$), higher channel lengths are required in the straight channel,
- for $0.2 < j_g < 0.4$ m/s, both channels lead to identical $X_{E=0.95}$
- for $j_g \geq 0.4$ m/s (confined bubbles with $L_b/l > 4$), the meandering channel provides the lowest $X_{E=0.95}$ (almost 1 m, i.e. four times the present length).

These findings show that the meandering channel is more competitive than the straight channel for the lowest j_g and above all for the highest j_g (in the slug-annular regime), as enabling the intensification of gas–liquid mass transfer while being the most compact.

4.3. Interfacial area and liquid-side mass transfer coefficient

In order to estimate interfacial areas between gas and liquid phases, a hemispherical shape for bubble nose and rear is assumed as well as a cylindrical shape for bubble body. This is

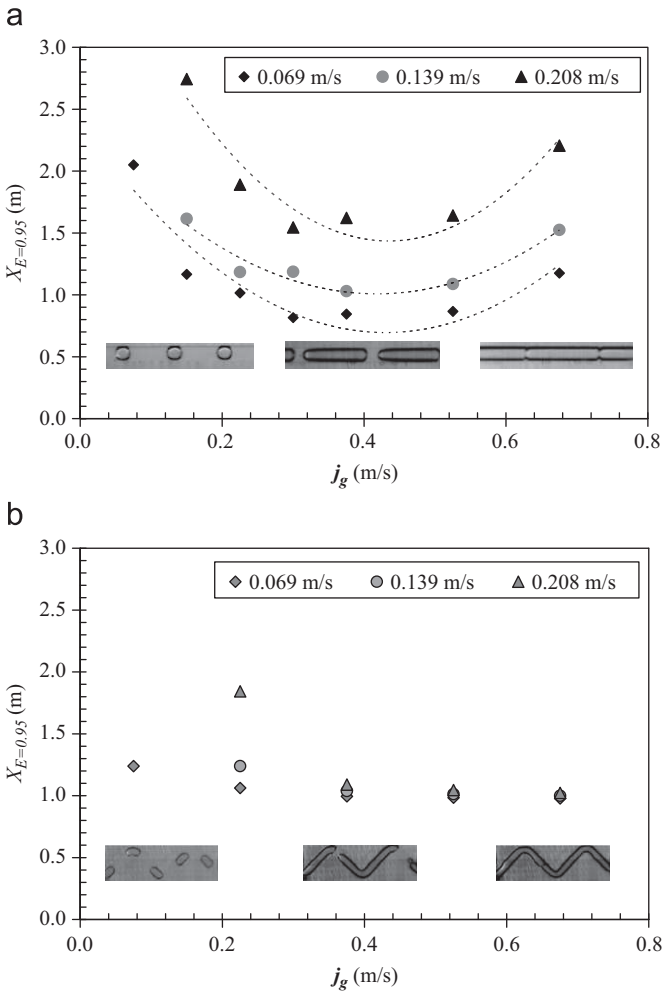

Fig. 15. Length of channel required to reach a liquid efficiency E of 0.95 versus gas superficial velocity for different liquid superficial velocities j_l (j_l=0.069 m/s: ◇; j_l=0.139 m/s: ○; j_l=0.208 m/s: Δ). (a) Straight channel and (b) meandering channel.

observed only in the Taylor regime (Figs. 4 and 5). Under the latter assumptions, the specific interfacial area for the liquid film a_f and the recirculating region a_r (Fig. 8) are given by

$$a_f = \frac{\pi(L_b-l)}{lL_{UC}} \tag{41}$$

$$a_r = \frac{\pi}{L_{UC}} \tag{42}$$

The total specific interfacial area ($a=a_f+a_r$) is plotted (only for the Taylor flow regime) as a function of gas superficial velocity in Fig. 16. A rise of a with increasing j_g and decreasing j_l is logically observed for both channels. The interfacial area a generated is slightly larger (5%) in the meandering channel than in the straight one, and vary from 150 to 1600 m^{-1}. The latter values are significantly higher than in usual gas–liquid macro-contactors, almost the same as in static mixers and smaller than in microchannels (Yue et al., 2007). All these findings are consistent with respect to the results already observed on bubble and slug sizes (Fig. 10). It is also interesting to notice that the increase of a with j_g is large, explaining thus the important variations of k_la with j_g reported in Fig. 13.

We now compare the experimental results for k_la with the theoretical calculations based on the fundamental model developed by van Baten and Krishna (2004). These authors proposed to

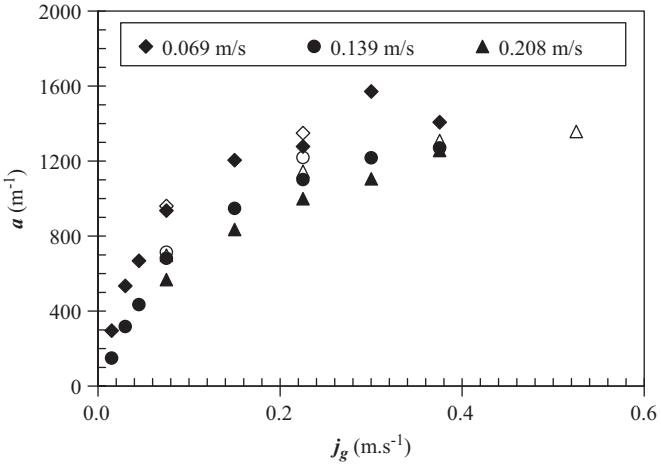

Fig. 16. Total specific interfacial area versus the gas superficial velocity for different liquid superficial velocities (j_l=0.069 m/s: ◇; j_l=0.139 m/s: ○; j_l=0.208 m/s: Δ). Dark and white symbols correspond to straight and meandering channels, respectively.

calculate liquid–side mass transfer coefficients from Higbie penetration's theory as

$$k_l = 2\sqrt{\frac{D}{\pi t_c}} \tag{43}$$

where t_c is the contact time between gas and liquid. In the liquid film area, it was defined by

$$t_{cf} = \frac{L_b - l}{U} \tag{44}$$

and in the recirculating region, by

$$t_{cr} = \frac{\pi l}{2U} \tag{45}$$

Considering the contribution of both interfacial areas, Eqs. (41)–(45) give

$$k_l a = k_{l,f} a_f + k_{l,r} a_r = 2\sqrt{\frac{2}{L_{UC}}}\sqrt{\frac{DU}{l}} + 2\sqrt{\frac{\pi(L_b - l)}{L_{UC} l}}\sqrt{\frac{DU}{L_b - l}} \tag{46}$$

The ratio between experimental and theoretical (deduced from Eq. (46)) volumetric mass transfer coefficients $k_l a$ is plotted in Fig. 17 as a function of gas superficial velocities. This figure shows that the model provides good orders of magnitude of $k_l a$, but clearly overestimates experimental values.

Because of the periodic contact of bubbles with the stagnant liquid film, it is reasonable to assume that the concentration of oxygen in the liquid film could saturate along the channel length. Di Miceli Raimondi et al. (2008) observed, in the case of droplets moving in a square microchannel in Taylor flow regime, that the length scale of liquid film saturation could be one order of magnitude shorter than the length scale of liquid slug saturation. Under these conditions, the contribution of bubble surface in contact with liquid film to mass transfer could be limited by oxygen saturation, explaining thus the overestimation of experimental $k_l a$ by the model of van Baten and Krishna (2004). To appreciate the relevancy of this assumption, the ratio between experimental $k_l a$ and the values deduced from Eq. (46) with neglecting mass transfer in the liquid film (first term) has been reported in Fig. 17. It is interesting to note that, for either of the channels and for $j_g > 0.1$ m/s, experimental $k_l a$ are bordered by the theoretical values calculated with and without taking into account mass transfer in the liquid film. For $j_g < 0.1$ m/s, the model without mass transfer in the liquid film always overestimates experimental results, but leads to $k_l a$ closer to

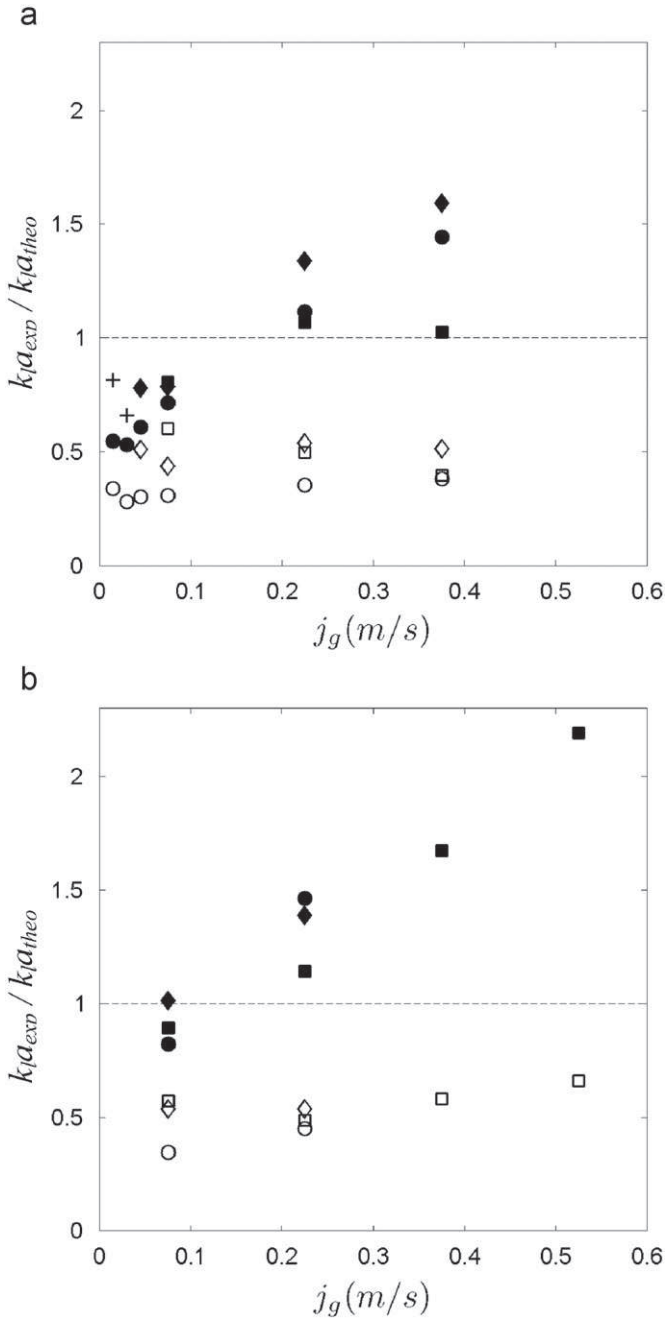

Fig. 17. Ratio between experimental and theoretical volumetric mass transfer coefficients (j_l=0.069 m/s: ○; j_l=0.139 m/s: ◇; j_l=0.208 m/s: □). Empty and dark symbols correspond to a modelling with and without accounting for mass transfer in the liquid film, respectively: (a) straight channel and (b) meandering channel.

experimental data than when mass transfer in the liquid film is considered. The discrepancy between theoretical and experimental $k_l a$ shows the inadequate and/or erroneous description of the mass transfer mechanisms through bubble surface in contact with liquid film. The main reason deals with the misunderstood dynamics of saturation of the liquid film along the channel length, dynamics due to the successive traffic of bubbles.

To appreciate the eventual saturation of the liquid film, the Fourier number is usually considered (for example, in Pohorecki, 2007):

$$Fo = \frac{t_c}{t_d} = \frac{L_b/U}{\delta^2/D} \tag{47}$$

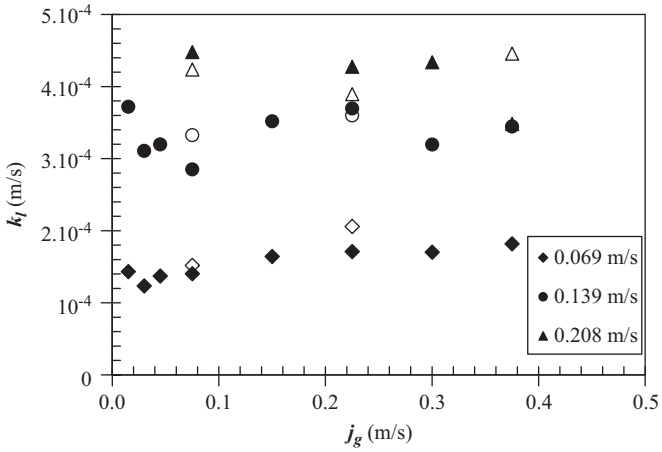

Fig. 18. Liquid-side mass transfer coefficients versus gas superficial velocity. (j_l=0.07 m/s: ◇; j_l=0.139 m/s: ○; j_l=0.208 m/s: Δ). Dark and white symbols correspond to straight and meandering channels, respectively.

where t_c and t_d are the contact time of the liquid film with bubbles and the diffusion time in the liquid film, respectively. As not measured in this study, the liquid thicknesses are estimated from the experimental results of Fries et al. (2008): for $10^{-3} < Ca < 10^{-2}$, the film thicknesses in the corner, δ_c, and at the wall, δ_w, are found equal to $2\delta_c/l \approx 0.15$ and to $2\delta_w/l \approx 0.02$, respectively. The diffusion times in the corner and at the wall are then $t_d^c = 9$ s and $t_d^w = 0.16$ s. Using the data from Figs. 10 and 11, the contact times are varying, for the straight channel from 0.0068 to 0.025 s, and for the meandering channel from 0.0075 to 0.027 s. Thus, the following ranges for Fourier number are deduced:

For the straight channel,

$$0.00043 < Fo^c < 0.016, \quad 0.042 < Fo^w < 0.156 \tag{48}$$

For the meandering channel,

$$0.00047 < Fo^c < 0.017, \quad 0.047 < Fo^w < 0.169 \tag{49}$$

The Fourier number involving the film thickness at the wall (Fo^w) remains below 0.2, suggesting thus that the contact time is too small to induce the saturation of the liquid film. Nevertheless, the question is whether such criterion is sufficient. Indeed, the liquid film being stagnant in most cases, it is not excluded that oxygen is progressively stored in the film as far as the bubbles are passing. The liquid film would thus not be fully saturated in the way of $C = C^*$, but an average of $0 < C_{film} < C^*$ would take place. On the other hand, if $2\delta_w/l$ is assumed varying between 0.01 and 0.03 instead of 0.02 (this is not unusual with respect to experimental uncertainties), Fo^w reaches then 0.7. This latter value, close to unity, shows that the film at the wall can be saturated while the part of liquid film in the corner is not ($Fo^c < 0.017$). These basic calculations confirm that a specific research effort should be made in the future to better understand and integrate this phenomenon in the modelling.

At last, liquid-side mass transfer coefficients, k_l, have been estimated by dividing experimental k_la to total interfacial area a: their variation with gas superficial velocity is plotted in Fig. 18. For both channels, k_l range between 10^{-4} and 5×10^{-4} m s^{-1}. These values have the same order of magnitude as those usually obtained in bubble columns or stirred tanks (Kies et al., 2004; Charpentier, 2001), but are three times smaller than the ones reached in microchannels (Yue et al., 2007). Fig. 18 also suggest that liquid-side mass transfer coefficients k_l would remain almost constant when increasing gas superficial velocities, would increase with increasing liquid superficial velocities and would not be affected by the presence of bends. Nevertheless, these trends should be analysed with caution due to experimental uncertainties, and especially to calculation approximations (in particular on the way to calculate total interfacial area).

5. Conclusion

Investigations on gas–liquid mass transfer were performed in square millimetric channels of different geometries, aiming at evaluating the benefits of meandering geometry with respect to straight channels. An original method was proposed based on the measurements of concentration of oxygen into deionised water along the channel length. It offered the advantage to verify the relevancy of the plug flow model, and thus to determine more accurately the volumetric mass transfer coefficients k_la.

Firstly, the use of a high speed camera enabled gas–liquid flows to be characterised. In the range of operating conditions ($0.015 \le j_g \le 0.675$ m/s, $0.069 \le j_l \le 0.208$ m/s), the usual flow regimes were encountered, namely Taylor flow regime (confined and unconfined bubbles) and slug-annular regime. The transition from the first to the second regimes was delayed in the meandering channel when compared to the straight channel. The comparison between the dimensionless numbers controlling the bubble shape (*Re*, *Ca*, *We*, *Bo* and *Ce*) revealed that inertial effects were dominant; the deformation of bubble from hemispherical ends to a more slender/flatter shape of nose/rear occurred approximately at $We = 1.5$ and was accentuated by the action of gravity and, in the meandering channel, by the presence of centrifugal forces. An analysis of flow structure indicated that, for the straight channel, the main part of the liquid phase was transported inside the recirculating region between two bubbles and that the liquid film could be reasonably considered as stagnant. For the Taylor regime, bubble lengths increased for increasing j_g and decreasing j_l ($0.8 < L_b/l < 6$), and using a meandering channel instead of a straight one enabled a rise of 10–20% in bubble lengths while conserving almost identical slug lengths. Whatever the channel, the bubble velocities were always larger than the total superficial velocities, demonstrating thus that a slip phenomenon between the bubbles and the liquid phase took place.

Secondly, the original method implemented for investigating mass transfer showed that the variation of volumetric mass transfer coefficients with gas superficial velocity depended on the nature of the flow regime. For the Taylor flows regime, k_la increased significantly when increasing j_g in both channels; this evolution was related to a large increase of the specific interfacial

area with j_g. Moreover, specific interfacial area, bubble velocity and volumetric mass transfer coefficient were just slightly higher in the meandering channel than in the straight one, indicating that the meandering geometry had no major impact on mass transfer for the Taylor flow. On the contrary, this influence was found no longer negligible for the slug-annular flow since, in the meandering channel, k_la were higher and became independent on j_g (they decreased with j_g in the straight channel). For either channel, the Number of Transfer Units in the liquid phase (NTU_l) remained low (close to one); thus, even if millimetric channels allowed gas–liquid mass transfer intensification (high k_la), a special attention should be paid for generating sufficient residence times. The calculation of the channel length necessary to reach an absorption efficiency of 95% revealed that the meandering channel was more competitive than the straight channel for the lowest j_g and above all for the highest j_g: indeed, it enabled to intensify gas–liquid mass transfer while being the most compact (the length required is smallest). At last, the discrepancy between experimental volumetric mass transfer coefficients k_la and those calculated from the model developed by van Baten and Krishna (2004) revealed that such modelling described inadequately mass transfer through bubble surface in contact with liquid film, mainly because of the saturation dynamics in the liquid film along the channel length.

In the future, this work should be completed for better understanding of the present results on mass transfer (contribution of liquid film, effect of channel bends). This will require experiments and/or numerical simulations to be carried out for accessing local velocity and concentration fields. For definite conclusions about the topic of meandering channels, measurements of gas–liquid mass transfer in presence of chemical reactions should also be run to investigate the influence of chemical kinetics on mass transfer (enhancement, reaction location).

Nomenclature

a	specific interfacial area (m^{-1})
A	cross-sectional area (m^2)
C	concentration in dissolved oxygen at the exit of the channel (kg/m^3)
C_{in}	concentration in dissolved oxygen at the inlet of the channel (kg/m^3)
C^*	concentration in dissolved oxygen at saturation (kg/m^3)
D	diffusion coefficient of oxygen in the liquid phase (m^2/s)
F	flux of liquid across a section of the channel (kg/s)
g	gravity acceleration (m/s^2)
G	gas molar flow rate (mol/s)
H	Henry constant (Pa)
j	total superficial velocity (Eq. (16)) (m/s)
k	mass transfer coefficient (m/s)
k_la	volumetric gas–liquid mass transfer coefficient (s^{-1})
K	overall mass transfer coefficient (m/s)
l	width of the channel (m)
L	liquid molar flow rate ($mol\ s^{-1}$)
L_b	length of the bubble (m)
L_{UC}	length of the unit cell (m)
m	Henry constant ($m=H/P$) (−)
P	pressure (Pa)
q	volumetric flow rate (m^3/s)
r_c	radius of curvature of the bend (meandering channel) (m)
t	time (s)
T	period of the gas–liquid flow (s)
U	bubble velocity (m/s)
V	liquid volume (m^3)
$V_{l,\ circ}$	volume of liquid passing through a transversal section of the channel during a period T (m^3)
W	relative slip velocity defined by Eqs. (18) and (19) (m/s)
X	location of gas injection from the exit of the channel (m)

Dimensionless numbers

Bo	Bond number (Eq. (3))
Ca	capillary number (Eq. (1))
Ce	non-dimensional number for centrifugal effects (meandering channel) (Eq (4))
E	liquid absorption efficiency (Eq. (38))
Fo	Fourier number (Eq. (47))
NTU	Number of Transfer Units (Eqs. (30), (33))
r	absorption ratio (Eq. (36))
Re	Reynolds number (Eq. (5))
We	Weber number (Eq. (2))

Greek letters

δ	liquid film thickness (m)
φ	volumetric flux of oxygen in the liquid ($kg\ s^{-1}\ m^{-3}$)
μ	dynamic viscosity (Pa s)
ρ	density (kg/m^3)
σ	surface tension (N/m)
τ	residence time for the liquid phase (s)

Subscripts

b	bubble
ex	exit of the channel
f	film
g	gas phase
in	inlet of the channel
l	liquid phase
r	liquid phase in the recirculating region (Fig. 8)
uc	Unit Cell

References

Annaland, M.V., Dijkhuizen, W., Deen, N.G., Kuipers, J.A.M., 2006. Numerical simulation of behavior of gas bubbles using a 3-D front-tracking method. AIChE Journal 52, 99–110.

Anxionnaz, Z., Cabassud, M., Gourdon, C., Tochon, P., 2008. Heat exchanger/reactors (HEX reactors): concepts, technologies: state-of-the-art. Chemical Engineering Process 47 (12), 2029–2050.

Anxionnaz, Z., 2009. Etude de l'influence de la géométrie des canaux sur les performnces d'un réacteur-échangeur. Thesis, University of Toulouse.

Anxionnaz, Z., Cabassud, M., Gourdon, C., Tochon, P., 2010. Transposition of an exothermic reaction from a batch reactor to an intensified continuous one. Heat Transfer Engineering 31 (9), 788–797.

Banerjee, S., Scott, D.S., Rhodes, E., 1970. Studies in cocurrent gas–liquid flow in helically coiled tubes. Part 11: theory and experiments on turbulent mass transfer with and without chemical reaction. Canadian Journal of Chemical Engineering 48, 542–551.

Barnea, D., Luninski, Y., Taitel, Y., 1983. Flow pattern in horizontal and vertical two-phase flow in small diameter pipes. Canadian Journal of Chemical Engineering 61, 617–620.

Barajas, A.M., Panton, R.L., 1993. The effect of contact angle on two-phase flow in capillary tubes. International Journal of Multiphase Flow 19 (2), 337–346.

Bercic, G., Pintar, A., 1997. The role of gas bubbles and liquid slug lengths on mass transport in the Taylor flow through capillaries. Chemical Engineering Science 52 (21,22), 3709–3719.

Bretherton, F.P., 1961. The motion of long bubbles in tubes. Journal of Fluid Mechanics 10, 166–168.

Charpentier, J.C., 2001. Mass-transfer rates in gas–liquid absorbers and reactors. Advances in Chemical Engineering 11, 1–133.

Di Miceli Raimondi, N., Prat, L., Gourdon, G., Cognet, P., 2008. Direct numerical simulations of mass transfer in square microchannels for liquid–liquid slug flow. Chemical Engineering Science 63, 5522–5530.

Ferrouillat, S., Tochon, P., Della Valle, D., Peerhossaini, H., 2006. Open loop thermal control of exothermal chemical reactions in multifunctional heat exchangers. International Journal Heat and Mass Transfer 49 (15–16), 2479–2490.
Fries, D.M., Trachsel, F., von Rohr, P.R., 2008. Segmented gas–liquid flow characterization in rectangular microchannels. International Journal of Multiphase Flow 34, 1108–1118.
Fries, D.M., Waelchli, S., von Rohr, P.R., 2009. Gas–liquid two-phase flow in meandering microchannels. Chemical Engineering Journal 135, S37–S45.
Garstecki, P., Fuerstman, M.J., Stone, H.A., Whitesides, G.M., 2006. Formation of droplets and bubbles in a microfluidic T-junction-scaling and mechanism of break-up. Lab on Chip 6, 437–446.
Giavedoni, M.D., Saita, F.A., 1999. The rear meniscus of a long bubble steadily displacing a Newtonian liquid in a capillary tube. Physics of Fluids 11 (4), 786–794.
Goel, D., Buwa, V.V., 2009. Numerical Simulations of Bubble Formation and Rise in Microchannels. Industrial & Engineering Chemistry Research 48, 8109–8120.
Hardt, S., Drese, K.S., Hessel, V., Schönfeld, F., 2005. Passive micromixers for applications in the microreactor and μTAS fields. Microfluid Nanofluid 1 (2), 108–118.
Hessel, V., Angeli, P., Gavriilidis, A., Löwe, H., 2005. Gas–liquid and gas–liquid–solid microstructured reactors: contacting principles and applications. Industrial & Engineering Chemistry Research 44, 9750–9769.
Higbie, R., 1935. The rate of absorption of a pure gas into a still liquid during short periods of exposure. Transactions of the AIChE 31, 365–389.
Irandoust, S., Andersson, B., 1988. Mass transfer and liquid-phase reactions in a segmented two-phase flow monolithic catalyst reactor. Chemical Engineering Science 43 (8), 1983–1988.
Jensen, M.J., Garstecki, P., Fuerstman, M., Bruns, H., Whitesides, G.M., Stone, H.A., 2005. Numerical and experimental investigation of bubble pinch-off in the flow-focusing device. Micro Total Analysis Systems 1, 626–628.
Kies, F.K., Benadda, B., Otterbein, M., 2004. Experimental study on mass transfer of a co-current gas–liquid contactor performing under high gas velocities. Chemical Engineering and Processing 43, 1389–1395.
Kreutzer, M.T., Kapteijn, F., Moulijn, J.A., Kleijn, C.R., Heiszwolf, J.J., 2003. Inertial and interfacial effects on pressure drop of Taylor flow in capillaries. AIChE Journal 51 (9), 2428–2440.
Kreutzer, M.T., Kapteijn, F., Moulijn, J.A., Heiszwolf, J.J., 2005. Multiphase monolith reactors: chemical reaction engineering of segmented flowin microchannels. Chemical Engineering Science 60, 5895–5916.
Laborie, S., Cabassud, C., Durand-Bourlier, L., Lainé, J.M., 1999. Characterisation of gas–liquid two-phase flow inside capillaries. Chemical Engineering Science 54, 5723–5735.
Lewis, W.K., Whitman, W.G., 1924. Principles of gas absorption. Industrial and Engineering Chemistry 16, 1215–1220.
Nguyen, N.-T., Wu, Z., 2005. Micromixers—a review. Journal of Micromechanics and Microengineering 15 (2), R1–R16.
Pohorecki, R., 2007. Effectiveness of interfacial area for mass transfer in two-phase flow in microreactors. Chemical Engineering Science 62, 6495.
Pohorecki, R., Kula, K., 2008. A simple mechanism of bubble and slug formation in Taylor flow in microchannels. Chemical Engineering Research and Design 86, 997–1001.
Qian, D., Lawal, A., 2006. Numerical study on gas and liquid slugs for Taylor flow in a T-junction microchannel. Chemical Engineering Science 61, 7609–7625.
Roustan, M., 2003. Transferts gaz-liquide dans les procédés de traitement des eaux et des effluents gazeux. Editions Dec & Doc Paris.
Shao, N., Gavriilidis, A., Angeli, P., 2010. Mass transfer during Taylor flow in microchannels with and without chemical reaction. Chemical Engineering Journal 160 (3), 873–881.
Sherwood, T.K., Pigford, R.L., Wilke, C.R., 1975. Mass Transfer. Mc-Graw Hill, New York, USA.
Sobieszuk, P., Cyganski, P., Pohorecki, R., 2010. Bubble lengths in the gas–liquid Taylor flow in microchannels. Chemical Engineering Research and Design 88, 263–269.
Stankiewicz, A., Moulijn, J., 2000. Process Intensification: Transforming Chemical Engineering. Chemical Engineering Progress 96 (1), 22–34.
Su, H., Wang, S., Niu, H., Pan, L., Wang, A., Hu, Y., 2010. Mass transfer characteristics of H_2S absorption from gaseous mixture into methyldiethanolamine solution in a T-junction microchannel. Separation and Purification Technology 72 (3), 326–334.
Taha, T., Cui, Z.F., 2006. CFD modelling of slug flow inside square capillaries. Chemical Engineering Science 61, 665–675.
Tan, J., Li, S.W., Wang, K., Luo, G.S., 2009. Gas–liquid flow in T-junction microfluidic devices with a new perpendicular rupturing flow route. Chemical Engineering Journal 146, 428–433.
Taylor, G.I., 1961. Deposition of a viscous fluid on the wall of a tube. Journal of Fluid Mechanics 10, 161–165.
Thulasidas, T.C., Abraham, M.A., Cerro, R.L., 1995. Bubble-train flow in capillaries of circular and square cross section. Chemical Engineering Science 50 (2), 183–199.
Thulasidas, T.C., Abraham, M.A., Cerro, R.L., 1997. Flow patterns in liquid slugs during bubble-train flow inside capillaries. Chemical Engineering Science 52 (17), 2947–2962.
Tortopidis, P., Bontozoglou, V., 1997. Mass transfer in gas–liquid flow in small-diameter tubes. Chemical Engineering Science 52, 2231–2237.
Van Baten, J.M., Krishna, R., 2004. CFD simulations of mass transfer from Taylor bubbles rising in circular capillaries. Chemical Engineering Science 59, 2535–2545.
Vandu, C.O., Liu, H., Krishna, R., 2005. Mass transfer from Taylor bubbles rising in single capillaries. Chemical Engineering Science 60, 6430–6437.
Van Steijn, V., Kreutzer, M.T., Kleijn, C.R., 2007. μ-PIV study of the formation of segmented flow in microfluidic T-junctions. Chemical Engineering Science 62, 7505–7514.
Weber, M.W., Shandas, R., 2007. Computational fluid dynamics analysis of microbubble formation in microfluidic flow-focusing devices. Microfluidics and Nanofluidics 3, 195–206.
Yue, J., Chen, G., Yuan, Q., Luo, L., Gonthier, Y., 2007. Hydrodynamics and mass transfer characteristics in gas–liquid flow through a rectangular microchannel. Chemical Engineering Science 62, 2096–2108.
Zhao, C.-X., Middelberg, A.P.J., 2010. Two-phase microfluidic flows. Chemical Engineering Science, doi: 10.1016/j.ces.2010.08.038.